

# Development of a Biomembrane Platform for the Study of Virus Infection

**CNF Project Number: 1686-08**

**Principal Investigator(s): Susan Daniel**

**User(s): Zhongmou Chao, Alexis Ostwalt, Jordan Fitzgerald, Eleanor Best**

*Affiliation(s): Smith School of Chemical and Biomolecular Engineering, Cornell University*

*Primary Source(s) of Research Funding: Defense Threat Reduction Agency*

*Contact: sd386@cornell.edu, zc83@cornell.edu*

*Research Group Website: <https://daniel.cbe.cornell.edu/>*

*Primary CNF Tools Used: Heidelberg DWL2000 Mask Writer, ABM Contact Aligner, Odd Hour E-beam Evaporator, Oxford PECVD, PT-740 etcher, Disco Dicing Saw, Bruker AFM*

## Abstract:

As a “label-free” alternative to optical sensing, electrical sensing represents a more feasible, reproducible, and scalable detection method [1,2]. Among various electrical sensing techniques, the non-invasive electrochemical impedance spectroscopy (EIS) technique is especially suitable for accurately quantifying the bio-recognition events occurring at a variety of biointerfaces, such as bacterial, viral, cellular and synthetic lipid membranes [3,4]. Our group aims to design a microelectrode system that will support the self-assembly of lipid vesicles (SLBs) on the electrode surfaces, and their electrical properties (resistance, capacitance) can be extracted by applying an alternating voltage and recording the current response [4-7]. We have recently demonstrated such platform can be used to recreate viral infection of host cell and can differentiate different virus mutations [8]. Future work plan to incorporate microfluidic system with the microelectrode system.

## Summary of Research:

To fabricate the microelectrode devices, photomasks were created using the Heidelberg DWL2000 Mask writer and used with the ABM Contact Aligner to pattern photoresist that was spun onto a fused silica wafer. A first layer of gold contact pad was patterned following the developing of S1813 photoresist and the deposition of Au thin film. A thin layer of SiO<sub>2</sub> insulating layer is then deposited directly on top of the Au contact pad using Oxford PECVD. Electrode area was then patterned on SiO<sub>2</sub> following the spin-coating and developing of the second layer of photoresist. PT-740 etched was then used to etch the exposed SiO<sub>2</sub> until Au contact pad has been exposed. A conductive polymer, PEDOT:PSS was then spun over the fused silica wafer followed by the deposition of a Germanium hard mask (odd hour e-beam evaporator). A third layer of photolithography

was performed on a layer of negative photoresist (nLOF 2020) spun on top of Ge, where all resists above Ge at areas except active electrode surface were developed. Unprotected Ge and PEDOT:PSS underneath were then etched using PT-740. Ge on top of active electrode area was then etched in water bath overnight.

Once the microelectrode device was fabricated, a PDMS well was stamped directly on top to create a reservoir for SLB self-assembly and allow following EIS measurement.

## References:

- [1] Berggren, Magnus, and Agneta Richter. Dahlfors. “Organic bioelectronics.” *Advanced Materials* 19.20 (2007): 3201-3213.
- [2] Chalklen, Thomas, Qingshen Jing, and Sohini Kar-Narayan. “Biosensors based on mechanical and electrical detection techniques.” *Sensors* 20.19 (2020): 5605.
- [3] Magar, Hend S., Rabeay YA Hassan, and Ashok Mulchandani. “Electrochemical Impedance Spectroscopy (EIS): Principles, Construction, and Biosensing Applications.” *Sensors* 21.19 (2021): 6578.
- [4] Lisdat, F., and D. Schäfer. “The use of electrochemical impedance spectroscopy for biosensing.” *Analytical and Bioanalytical Chemistry* 391.5 (2008): 1555-1567.
- [5] Tang, Tiffany, et al. “Functional infectious nanoparticle detector: Finding viruses by detecting their host entry functions using organic bioelectronic devices.” *ACS Nano* 15.11 (2021): 18142-18152.
- [6] Bint E Naser, Samavi Farnush, et al. “Detection of Ganglioside-Specific Toxin Binding with Biomembrane-Based Bioelectronic Sensors.” *ACS Applied Bio Materials* 4.11 (2021): 7942-7950.
- [7] Pappa, Anna-Maria, et al. “Optical and electronic ion channel monitoring from native human membranes.” *ACS Nano* 14.10 (2020): 12538-12545.
- [8] Chao, Zhongmou, et al. “Recreating the biological steps of viral infection on a cell-free bioelectronic platform to profile viral variants of concern.” *Nature Communications* 15.1 (2024): 5606.



# Metamaterial Elliptical Cylinder for High Sensitive Single-Molecule Torque Detection

**CNF Project Number: 1738-08**

**Principal Investigator(s): Michelle D. Wang**

**User(s): Yifeng Hong**

*Affiliation(s): Department of Electrical and Computer Engineering, Cornell University;  
Department of Physics, Cornell University; Howard Hughes Medical Institute*

*Primary Source(s) of Research Funding: Howard Hughes Medical Institute*

*Contact: mdw17@cornell.edu, yh874@cornell.edu*

*Research Group Website: <http://wanglab.lassp.cornell.edu/>*

*Primary CNF Tools Used: ASML Deep Ultraviolet Stepper, Oxford 81 Etcher, Oxford 82 Etcher, Oxford PECVD, SC4500 Odd-Hour Evaporator, SC4500 Even-Hour Evaporator, Zeiss Supra SEM, Zeiss Ultra SEM*

## Abstract:

To facilitate the single-molecule torque measurement with the angular optical trap (AOT), we designed and fabricated novel metamaterial elliptical cylinders for higher torque resolution. By designing the cylinders to a smaller size, the torque resolution was improved over standard existing technique (quartz cylinders). The linear and angular trapping stiffness of the metamaterial elliptical cylinder can be controlled by tuning the mixing ratio of  $\text{SiO}_2$  and  $\text{Si}_3\text{N}_4$  to effectively modify the refractive index of the cylinder. These metamaterial elliptical cylinders can improve the utility of the AOT in investigating DNA-protein interactions.

## Summary of Research:

Torsional stress results in one of the main topological challenges in cells and plays an important role in fundamental biological processes, for example transcription and replication. In replication, torsion can accumulate both upstream and downstream of the replication fork. We are specifically interested in how DNA responds to torsion and what kinds of DNA structures form in response to topological changes. To quantitatively study these questions, our lab developed the angular optical trap (AOT) to measure torque at the single-molecule level [1-3]. As a standard configuration of the AOT, linearly polarized light is used to trap and rotate a birefringent particle anchored with a torsionally constrained DNA molecule for manipulation and measurement [2,3].

Historically, functionalized nanofabricated quartz cylinders ( $n_e = 1.54$  and  $n_o = 1.53$  at 1064 nm) with typical dimensions of diameter  $D \sim 500$  nm and height  $H$

$\sim 1000$  nm were utilized to simultaneously apply force and rotation to an attached DNA molecule for extension and torque measurements [2].

To facilitate the torque detection and allow better resolution, a smaller sample is required. However, a smaller quartz cylinder has a lower linear/angular trapping stiffness, resulting in the necessity of using high laser power, which may cause photodamage to a biological substrate [4].

To bypass this issue, we designed and fabricated multilayered elliptical cylinders with an effectively higher refractive index and a  $\sim 3$ -fold volume reduction in comparison to the previous quartz cylinders. These changes increased the torque resolution while maintaining strong linear/angular trapping stiffness. These cylinders were composed of silicon dioxide  $\text{SiO}_2$  ( $n_1 = 1.45$  at 1064 nm) and silicon nitride  $\text{Si}_3\text{N}_4$  ( $n_2 = 2.01$  at 1064 nm) (Figure 1), effectively resulting in a metamaterial [5].

As one can tell from the tensor (Figure 1), this metamaterial did not have birefringent effect at the  $xy$ -plane, thus we introduced shape anisotropy (i.e. utilizing elliptical shape) to generate torque for AOT manipulation (Figure 2).

## Conclusions and Future Steps:

These metamaterial elliptical cylinders have a decreased  $\gamma_\theta$  over our existing quartz cylinders, which facilitates an increased torque resolution for single-molecule AOT experiments. We believe these cylinders can have a significant impact on DNA torsional studies.

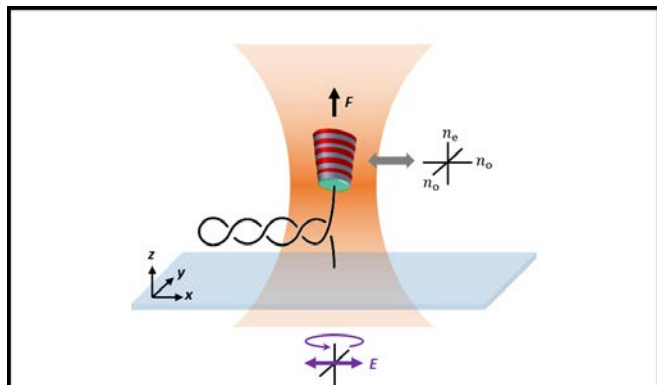


Figure 1: Experimental configuration of winding a DNA molecule with a metamaterial elliptical nanocylinder on the AOT. The long axis tends to align to the beam polarization when the beam is rotated.

### References:

- [1] La Porta, A. and M.D. Wang, Optical Torque Wrench: Angular Trapping, Rotation, and Torque Detection of Quartz Microparticles. *Physical Review Letters*, 2004. 92(19): p. 190801.
- [2] Deufel, C., et al., Nanofabricated quartz cylinders for angular trapping: DNA supercoiling torque detection. *Nature Methods*, 2007. 4(3): p. 223-225.
- [3] Gao, X., et al., Torsional Stiffness of Extended and Plectonemic DNA. *Physical Review Letters*, 2021. 127(2): p. 028101.
- [4] Neuman, K.C., et al., Characterization of Photodamage to Escherichia coli in Optical Traps. *Biophysical Journal*, 1999. 77(5): p. 2856-2863.
- [5] Cai, W. and V.M. Shalaev, *Optical metamaterials: fundamentals and applications*. 2010, New York: Springer. xii, 200 p.

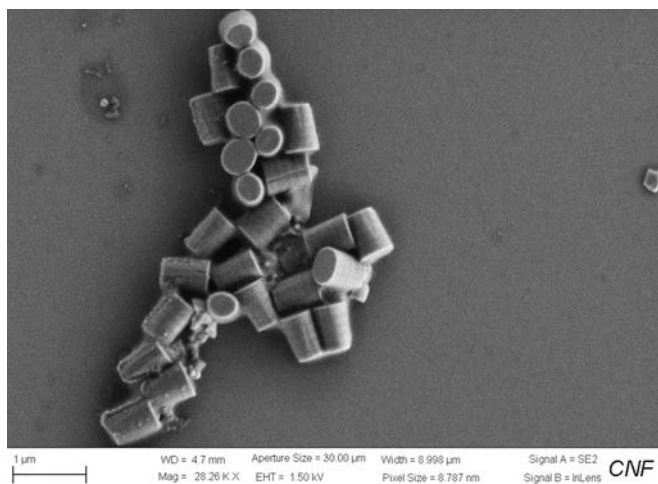


Figure 2: A scanning electron microscope image of metamaterial elliptical cylinders.

## Building Microfluidics Devices to Study Zinc Metal Homeostasis in *E. Coli* Communities

**CNF Project Number: 1844-09**

**Principal Investigator(s): Peng Chen**

**User(s): Felix Alfonso**

*Affiliation(s): Department of Chemistry and Chemical Biology, Cornell University*

*Primary Source(s) of Research Funding: National Institute of Health, the National Institute of General Medical Sciences*

*Contact: pc252@cornell.edu, fsa33@cornell.edu*

*Research Group Website: <http://chen.chem.cornell.edu/>*

*Primary CNF Tools Used: Heidelberg Mask Writer DWL2000, SUSS MA6-BA6 Contact Aligner, Oxford Cobra ICP Etcher, Plasma-Therm Deep Silicon Etcher, P7 Profilometer*

### Abstract:

Microbial life has a set of molecular tools to import essential nutrients from the surrounding environment and when necessary, efflux the excess to prevent harmful toxicity. The aim of this study is to elucidate the role individual bacterial cells play in achieving metal homeostasis at the community level. With this in mind, we engineered a custom microfluidic device that facilitates the controlled growth of *Escherichia coli* (*E. coli*) colonies within well-defined microchambers. These chambers' dimensions are carefully matched to the diameter of *E. coli* cells, thereby allowing for strategic cellular confinement — a critical aspect of our investigative method. The microfluidic devices we employed exhibit dynamic environmental control features, enabling us to switch solutions rapidly for stable, pulse, or step-function nutrient exposure as well as the creation of nutrient gradients. We employed advanced molecular biology techniques to engineer *E. coli* strains equipped with fluorescent protein reporters. This unique genetic modification allowed us to visualize and quantify gene expressions linked to the intricate influx and efflux ion channels, with particular emphasis on those specific to zinc. The insights derived from this study could have profound implications for our understanding of microbial ecosystems and their interactions with the environment.

### Summary of Research:

Zinc, a fundamental micronutrient, is indispensable for all living organisms [1]. It serves vital functions in protein folding, catalysis, and gene regulation [2,3]. An imbalance in zinc levels, either a deficiency or an excess, can trigger substantial alterations in the gut microbiome, thereby resulting in adverse health conditions [4,5]. Microbes have developed molecular mechanisms to

efficiently import nutrients from the environment and efflux under excess. To regulate these efflux pumps, bacteria modulate the transcription of protein pumps using metal-responsive transcription regulators. These regulators monitor the cellular concentration of metal ions, guiding cells towards achieving an optimal state of metal homeostasis.

Our project is designed to explore and quantify the management of  $Zn^{2+}$  within a microbiome, shedding light on the role individual cells assume in establishing community-wide metal homeostasis. We have chosen *Escherichia coli* (*E. coli*) as our model organism to investigate the complexities of community-derived zinc metal regulation. *E. coli*'s natural motility and poor adherence to substrates present challenges for long-duration imaging studies. However, microfluidics technology offers an effective solution, providing a controlled environment conducive to studying bacterial communities [6]. A microfluidic platform permits tight control of the nutrients influx and has been successfully used for long-timescale imaging studies [7]. The microfluidic device employed in our study is engineered

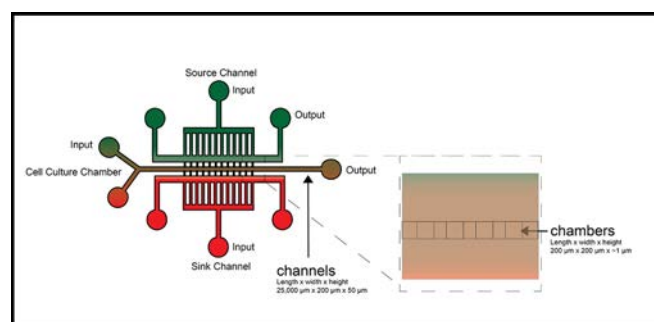


Figure 1: Schematic of gradient generating microfluidic device showing the source and sink channels and the chamber.

with three key components: a gradient generator, channels, and microchambers. The microchambers' depth is tailored to match the diameter of an E. coli cell ( $\sim 1 \mu\text{m}$ ), thereby facilitating the efficient confinement of colonies. The gradient generator was designed with the goals of creating a stable concentration gradient and minimization of convection inside the chambers. The design presented by E. Bernson, and A. Shamloo provided an optimal method to create a stable gradient inside the chamber (Figure 1, 8-9). This is accomplished by having a source chamber and a sink chamber. The molecule of interest diffuses through the microcapillaries that connect the source and sink to the main culture chamber.

The construction of these microfluidic devices relies on established silicon nanofabrication technology. The fabrication scheme is summarized in Figure 2. The fabrication process begins with silicon wafers being cleaned with piranha solution. They are then coated with photoresists, which are removed 2 mm from the wafer's edge using an edge bead removal system. The substrate is patterned using a pre-designed photomask created with the Heidelberg Mask Writer DWL2000. The Karl SUSS MA6-BA6 contact aligner provides UV light exposure for the wafer, which is developed and cleaned with a brief oxygen plasma treatment. Chambers are created by etching approximately  $\sim 1 \mu\text{m}$  of silicon using the Oxford Cobra ICP Etcher, and then the photoresist is removed with a stripper bath. The chamber's height is measured using a profilometer. Channel construction involves the use of SU-8 lithography, where SU-8 is spin-coated onto the substrate and patterned with the Karl SUSS MA6-BA6 contact aligner. After a curing

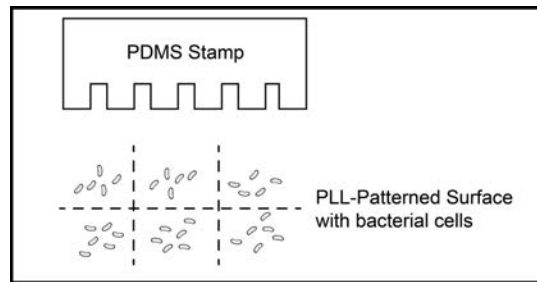


Figure 3: Patterning of the coverslip surface using PDMS stamps coated with PLL.

phase on a hot plate at  $95^\circ\text{C}$ , the unpolymerized SU-8 is removed with the developer. The resulting structure is then hard baked for 10 minutes at  $200^\circ\text{C}$ . The final step entails coating the silicon mold with a hydrophobic molecular monolayer such as tridecafluoro-1,1,2,2-tetrahydrooctyl trichlorosilane (FOTS) to facilitate PDMS removal. After casting PDMS on the silicon mold, the microfluidic devices are bonded to coverslips and inspected under a microscope. Cells are loaded into the chambers and imaged with a microscope equipped with the appropriate laser line and filters. Currently, we are exploring new methods to load the bacterial cells into the microchambers such as patterning the surface of the coverslip using PDMS stamps coated with PLL (Figure 3). The overall goal is to pattern the surface with cells to match the geometry of microfluidic devices to achieve better spatially distributed cells.

### References:

- [1] R. R. Robert B. Saper, Zinc: An Essential Micronutrient. *Am. Fam. Physician.* 79, 768 (2009).
- [2] S. Tan, D. Guschin, A. Davalos, Y.-L. Lee, A. W. Snowden, Y. Jouvenot, H. S. Zhang, K. Howes, A. R. McNamara, A. Lai, C. Ullman, L. Reynolds, M. Moore, M. Isalan, L.-P. Berg, B. Campos, H. Qi, S. K. Spratt, C. C. Case, C. O. Pabo, J. Campisi, P. D. Gregory. *Proc. Natl. Acad. Sci. U. S. A.* 100, 11997-12002 (2003).
- [3] C. Andreini, I. Bertini, in *Encyclopedia of Metalloproteins* (Springer, New York, NY, 2013), pp. 2549-2554.
- [4] S. R. Gordon, S. Vaishnav. *The Journal of Immunology.* 204, 83.18-83.18 (2020).
- [5] O. Koren, E. Tako. *Proc. AMIA Annu. Fall Symp.* 61, 16 (2020).
- [6] F. Wu, C. Dekker. *Chem. Soc. Rev.* 45, 268-280 (2016).
- [7] D. Binder, C. Probst, A. Grünberger, F. Hilgers, A. Loeschke, K.-E. Jaeger, D. Kohlheyer, T. Drepper. *PLoS One.* 11, e0160711 (2016).
- [8] E. Bernson, Development of a Microfluidic Platform for Cell migration Studies along Gradients (2012) (available at <https://odr.chalmers.se/items/8199a5e9-f3f0-4824-9056-51f603dcfd7d>).
- [9] A. Shamloo, N. Ma, M.-M. Poo, L. L. Sohn, S. C. Heilshorn. *Lab Chip.* 8, 1292-1299 (2008).

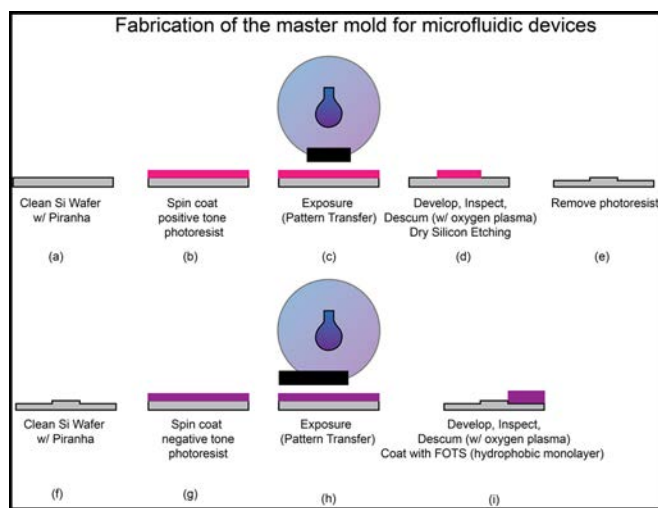


Figure 2: Fabrication of microfluidic devices combining dry etching to construct the chambers and SU-8 lithography to construct the channels.

# Design and Application of Microfluidic Devices to Study the Effect of the Physical Microenvironment on Cellular Function

**CNF Project Number: 2065-11**

**Principal Investigator(s): Jan Lammerding**

**User(s): Richa Agrawal, Maggie Elpers, Eitan Jentis, Sarah Henretta**

*Affiliation(s): Meinig School of Biomedical Engineering,  
Weill Institute for Cell and Molecular Biology; Cornell University*

*Primary Source(s) of Research Funding: NIH award R01 GM137605; NIH award R01 HL082792;  
NIH award R35 GM153257; NIH award 1U54 CA261694*

*Contact: jan.lammerding@cornell.edu, ra664@cornell.edu,  
mae228@cornell.edu, ej225@cornell.edu, sjh333@cornell.edu*

*Research Group Website: <http://lammerding.wicmb.cornell.edu/>*

*Primary CNF Tools Used: PT 770, Oxford Cobra, Heidelberg DWL 2000 Mask Writer, Karl Suss MA6,  
Anatech SCE-110-RF Resist Stripper, P-7 Profilometer, MVD 100, Oxford 81, Unaxis 700, EcoClean tool*

## Abstract:

The physical environment of cells directly modulates their function and fate. Using microfabricated devices that mimic the confined spaces within tissues, we previously demonstrated that cell migration through tight spaces is limited by the deformability of the large cell nucleus, and that the physical stress associated with such ‘confined migration’ can result in nuclear envelope rupture, DNA damage, and changes in chromatin organization [1-5]. As part of this project, we applied our microfluidic devices to study confined migration, identifying a novel mechanism by which cells squeeze their nucleus through small spaces [6], while also developing novel devices to enable the collection of large numbers of cells that have completed confined migration for genomic and transcriptomic analysis. Additionally, we developed a novel device to precisely confine cells to specific heights with micron resolution [7]. Expanding our mechanobiology research into another direction, we have begun developing microstructured surfaces that promote differentiation of cardiac and skeletal muscle stem cells into more mature muscle cells, thus enabling us to study the effect of disease-causing mutations on muscle function.

## Research Summary:

During *in vivo* migration, immune cells, fibroblasts, or metastatic tumor cells traverse interstitial spaces as small as 1-2  $\mu\text{m}$  in diameter. This ‘confined migration’ requires the deformation not only of the soft cell body but also the rate-limiting step of deforming the relatively rigid nucleus [1]. To study these processes in more detail, we have previously designed and fabricated polydimethyl siloxane (PDMS) microfluidic devices to

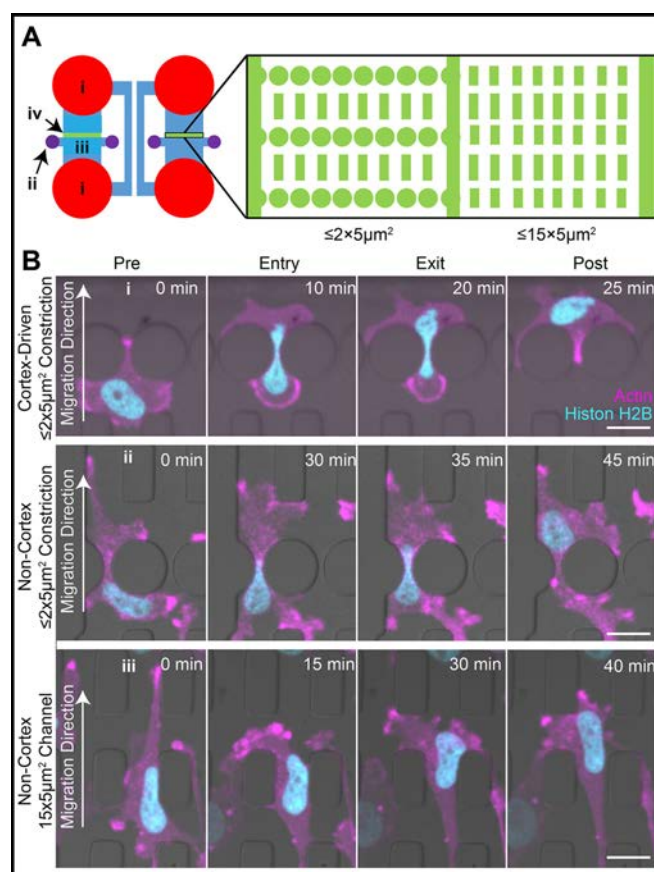
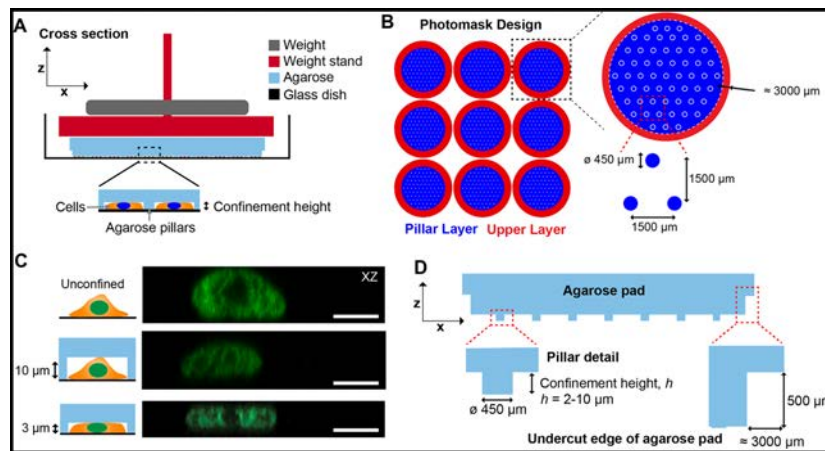


Figure 1: Microfluidic migration device to study confined migration mechanisms. (A) Overview of microfluidic migration device. (B) Time-lapse microscopy sequence of cells migrating through confined spaces using rear cortex contraction (top) or nuclear pulling (center and bottom) mechanism. Figure panels reproduced from Keys, et al. [7].

model the confined spaces that cancer cells may encounter during the metastatic process (Figure 1A) [8]. Using time-lapse imaging of cells expressing fluorescently labeled cytoskeletal components, we identified that cells can either use a ‘nuclear pulling’ mechanism, in which contraction of actomyosin fibers pull the nucleus through the tight space, or a ‘rear cortex contraction’ mechanism, in which contraction of the back of the cell generates a hydrostatic pressure gradient within the cell that drives the nucleus through the constriction (Figure 1B). We confirmed the biophysical mechanisms using laser ablation and fluorescent reporters. This work was recently published in the *Journal of Cell Science* [6].

Since the previous generation of microfluidic devices could not collect sufficient numbers of cells that have migrated through the confined spaces to perform biochemical or sequencing-based analyses, we designed novel migration devices that enable collection of 1000’s of cells post confined migration. We optimized several fabrication steps for these devices, including etching with hydrogen bromide in the Oxford Cobra etcher to achieve vertical device features in the mold for the PDMS microfluidic devices. We are currently in the process of applying these devices to analyze the effect of confined migration on gene expression and changes in chromatin organization in cancer cells.

In addition to the migration devices, we also developed a cell confinement device (Figure 2), in which we can precisely confine cells using an agarose pad containing micro-pillars fabricated to the height of interest (i.e., 3-15  $\mu\text{m}$ ). To make the device, agarose is cast onto a mold consisting of a silicon wafer fabricated to contain the negatives of the desired pillar features, and the agarose device is cut out and placed onto cells seeded on a glass-bottomed dish. The silicon wafer is fabricated using photolithography with SU-8 photoresist. We have fabricated devices with various heights to induce different degrees of confinement. The devices are suitable for short- and long-term confinement studies and compatible with imaging of both live and fixed samples. This work was recently published in *Current Protocols in Cell Biology* [5]. We are currently applying these devices to assess the effect of confinement on polarization and gene expression in primary bone marrow-derived macrophages.



*Figure 2: Agarose-based cell confinement device. (A) Cross section (left) schematic of the confinement device assembly. Assembly includes a glass bottomed dish (black), agarose device (blue), weight holder (red), and weight (gray). (B) Overlay of the lower- and upper-layer photomask designs showing the array of micropillars for one confinement device. (C) Representative images of breast cancer cells with nuclei fluorescently labeled with histone 2B-mNeonGreen under either unconfined, confined to 10  $\mu\text{m}$ , or confined to 3  $\mu\text{m}$  conditions. Scale bars: 10  $\mu\text{m}$ . (D) Schematic depiction of a single agarose device. Figure adapted from Elpers, et al. [5].*

Lastly, we recently designed microstructured substrates consisting of approximate 800 nm x 800 nm (W x H) ridges that promote alignment and maturation of muscle cells grown on them. To fabricate the structures, OiR620-7i photoresist was spun onto silicon wafers and exposed using the i-line stepper. Next, the Oxford 81 etcher was used to perform a descum process to prepare the wafer for deep silicon etching. The Unaxis 700 Deep Silicon Etcher was used to etch ca. 800 nm into the silicon. Excess photoresist is stripped using the EcoClean tool, and a FOTS coating is applied using the MVD 100 so that a PDMS cast can be made of the wafer, which then serves as the actual microstructured substrate for the cells. The transparent and flexible PDMS allows for imaging cells through the substrate, and also for applying uniaxial strain to the substrate, mimicking muscle contraction.

Taken together, these examples illustrate new uses of the available nanofabrication technologies to create improved in vitro models to study confined cell migration and mechanobiology.

## References:

- [1] Davidson, P., et al. *Cell Mol Bioeng*, 2014. 7(3): p. 293-306.
- [2] Bell, E.S., et al. *Oncogene*, 2022. 41(36): p. 4211-4230.
- [3] Denais, C.M., et al. *Science*, 2016. 352(6283): p. 353-8.
- [4] Shah, P., et al. *Curr Biol*, 2021. 31(4): p. 753-765 e6.
- [5] Hsia, C.R., et al. *iScience*, 2022. 25(9): p. 104978.
- [6] Keys, J., et al. *J Cell Sci*, 2024. 137(12).
- [7] Elpers, M.A., et al. *Curr Protoc*, 2023. 3(7): p. e847.
- [8] Davidson, P.M., et al. *Integr Biol*, 2015. 7(12): p. 1534-46.

# Metasurface-Enhanced Mid-Infrared Microscopy for Imaging Living Cells

**CNF Project Number: 2472-16**

**Principal Investigator(s): Gennady Shvets**

**User(s): Steven He Huang, Po-Ting Shen**

*Affiliation(s): Applied and Engineering Physics, Cornell University*

*Primary Source(s) of Research Funding: National Cancer Institute of the National Institutes of Health award number R21 CA251052. National Institute of General Medical Sciences of NIH award number R21 GM138947*

*Contact: gs656@cornell.edu, hh623@cornell.edu, ps944@cornell.edu*

*Research Group Website: <http://shvets.aep.cornell.edu>*

*Primary CNF Tools Used: JEOL 9500, SC4500 Evaporator, Zeiss Supra SEM, PDMS Casting Station, Anatech Resist Strip, Glen 1000 Resist Strip, DISCO Dicing Saw*

## Abstract:

We have developed Metasurface-Enhanced Mid-Infrared Microscopy (MEMIM) as a novel tool for chemical imaging of living cells. In MEMIM, cells are cultured on an array of plasmonic nanoantennas (metasurface), and their near-field interaction alters the scattering cross-section of the nanoantennas, making the cells visible in the far field. The imaging contrast arises from the mid-infrared vibrational absorption of the cells, primarily originating from the major classes of biomolecules including DNA, proteins, and lipids. Our technology is a label-free, non-destructive imaging technique with chemical contrast, holding wide potential applications in biomedical research.

## Summary of Research:

Infrared (IR) spectroscopy and chemical imaging are widely used to identify chemical compounds through their molecular vibration fingerprints and has found many applications in biological analysis. Yet, the use of IR microscopy for imaging living cells is challenging due to the attenuation of IR light in water, necessitating the use of thin flow cells or attenuated total reflection (ATR) configurations that are difficult to scale to high-throughput measurements. In the past, we have used plasmonic metasurfaces to overcome this challenge, demonstrating the spectroscopic measurement of changes related to cell adhesion and dissociation, cholesterol depletion, and activation of intracellular signaling pathways [1,2]. Recently, we have expanded this technique to a novel chemical imaging technique, called MEMIM, to image living cells in physiological conditions. In MEMIM, cells are grown on an array of resonant plasmonic nanoantennas called metasurfaces. These resonant nanoantennas interact with the cells in the near-field through their plasmonic hotspots, in

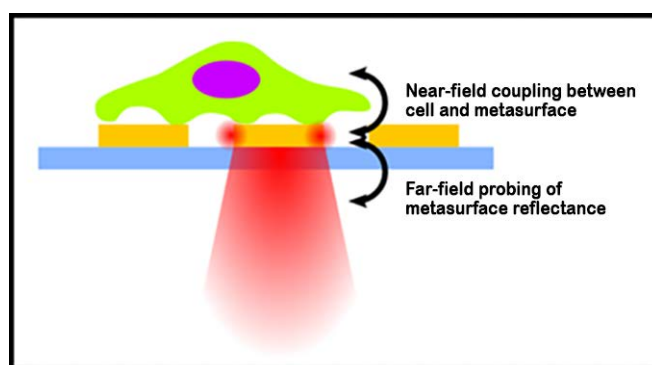


*Figure 1: Metasurface-enhanced infrared spectroscopy and chemical microscopy. The near-field interaction of cells with metasurface results in SEIRA, which changes the scattering cross section of the individual nanoantennas. This interaction is probed in the far-field via metasurface reflectance, allowing for non-perturbative infrared spectroscopy of living cells.*

an effect called surface-enhanced infrared adsorption (SEIRA), leading to a modulation in the far-field scattering cross-section of the nanoantennas. Images of analytes on the metasurface are formed by a mid-infrared laser scanning microscope, focused to the plane of the metasurface (Figure 1).

Our mid-IR metasurface is fabricated as an array of gold nanoantennas on IR transparent CaF<sub>2</sub> substrates (0.5 mm thick). The substrate is first cleaned using oxygen plasma etcher (Anatech or Glen 1000 Resist Strip). Metasurface patterns are defined using electron beam lithography with the JEOL 9500 system and poly(methyl methacrylate) (PMMA) as the resist. 5 nm Cr adhesion layer and 70 nm Au are deposited using SC4500 evaporator. As the final step, oxygen plasma etcher (Anatech or Glen 1000 Resist Strip) is used to clean the metasurface sample. The metasurface is then attached to superstructures for cell culture chambers and cells are grown on top of the metasurface.

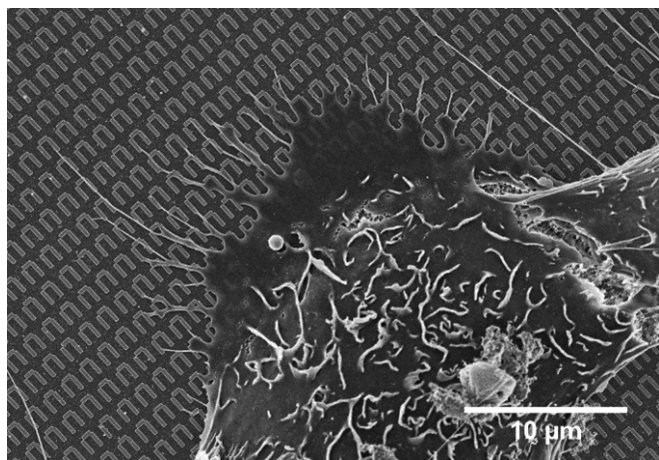


Figure 2: Scanning electron microscope image of a A431 human skin cancer cell on the metasurface. Scale bar: 10  $\mu\text{m}$ .

Figure 2 shows a scanning electron microscope image of a cell on the metasurface.

Our group recently designed and built an inverted point-scanning confocal microscope using a mid-IR quantum cascade laser (QCL) light source. The emission from a QCL is focused on a diffraction-limited spot on the metasurface and scanned across it by moving the sample with a motorized microscope stage. The reflection, modulated by the metasurface's near-field interaction with the analyte, is collected by a liquid-nitrogen-cooled mercury-cadmium-telluride (MCT) mid-IR detector. The lateral resolution of our imaging system is diffraction-limited to about 5  $\mu\text{m}$ .

Using this setup, we have demonstrated the efficacy of MEMIM for label-free imaging of both fixed and living cells on the metasurface. Images of fixed 3T3-L1 fibroblasts (pre-adipocytes), shown in Figure 3, reveal clear chemical contrast from proteins (amide I/II bands, 1500-1700  $\text{cm}^{-1}$ ) and DNA (PO<sub>2</sub>- phosphate bands, 1085  $\text{cm}^{-1}$ ). Comparison with fluorescent images shows good correlation, with phosphate band IR images aligning well with nucleus-stained fluorescence images. The protein IR image also matches the actin-

stained fluorescence image, capturing the cell's outer morphology, although differences arise because the protein IR image includes all proteins, not just actin. Lipid droplets in differentiated 3T3-L1 adipocytes can also be imaged through the C=O ester carbonyl vibration of the lipids at 1740  $\text{cm}^{-1}$  (image not shown). We also performed time-lapse imaging of living cells (data not shown) to monitor cell adhesion and motility on the metasurface. These live cell imaging results confirm that living cells can be imaged using our technique without affecting cell viability and behavior under mid-IR light.

## Conclusions and Future Steps:

We have developed a plasmonic metasurface-based mid-infrared chemical imaging technology for the label-free, non-destructive imaging of living cells with chemical contrast. Imaging cells with contrast arising from proteins, DNAs, and lipids have been demonstrated. This technique could allow for the non-perturbative metabolic imaging of living cells over several days, which is currently not possible using other similar techniques. We plan to expand this technology to the metabolic imaging of cells using small IR-active metabolic labels, such as azides, deuterium, and <sup>13</sup>C. This could help in characterizing heterogeneity in metabolic rates within the cell population and how they are changed through drug treatment or other environmental cues, with implications in metabolic diseases such as diabetes and fatty liver diseases.

## References:

- [1] Huang, S. H., et al. Monitoring the effects of chemical stimuli on live cells with metasurface-enhanced infrared reflection spectroscopy. *Lab Chip* 21, 3991-4004 (2021).
- [2] Huang, S. H., et al. Metasurface-enhanced infrared spectroscopy in multiwell format for real-time assaying of live cells. *Lab Chip* 23, 2228-2240 (2023).

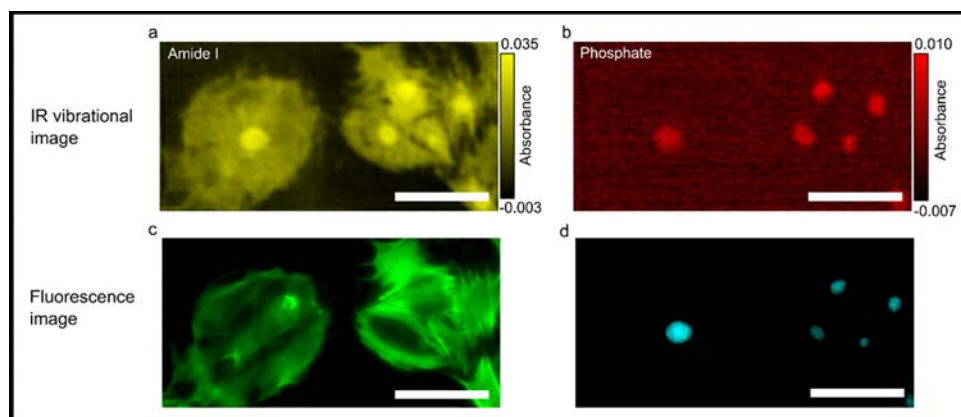


Figure 3: Metasurface-enhanced IR chemical microscopy of fibroblasts. (a): IR vibrational image at amide I band (1655  $\text{cm}^{-1}$ , contrast from total proteins). (b): IR vibrational image at phosphate band (1085  $\text{cm}^{-1}$ , contrast from DNA). (c): Actin-stained fluorescent image. (d): Nucleus-stained fluorescent image. Scale bar: 100  $\mu\text{m}$ .

# Time-Lapse Mid-Infrared Spectroscopy of Live Cells Using High-Aspect-Ratio Metal-on-Dielectric Nanostructures

**CNF Project Number: 2472-16**

**Principal Investigator(s): Gennady Shvets**

**User(s): Aditya Mahalanabish, Dias Tulegenov**

*Affiliation(s): Applied and Engineering Physics, Cornell University*

*Primary Source(s) of Research Funding: National Cancer Institute of the National Institutes of Health award number R21 CA251052; National Institute of General Medical Sciences of the NIH award number R21 GM138947*

*Contact: gshvets@cornell.edu, am2952@cornell.edu, dt483@cornell.edu*

*Research Group Website: <http://shvets.aep.cornell.edu>*

*Primary CNF Tools Used: JEOL 9500, SC4500 Evaporator, Zeiss Ultra Scanning Electron Microscope, Oxford Plasma Enhanced Chemical Vapor Deposition, Plasma-Therm 740, Anatech Resist Strip, DISCO Dicing Saw*

## Abstract:

Our group previously introduced Metasurface-Enhanced Infrared Spectroscopy (MEIRS) for spectral analysis and chemical imaging of live cells. MEIRS uses plasmonic nanoantenna arrays (metasurfaces) to enhance infrared signals by coupling molecular vibrations to plasmonic resonances. However, flat plasmonic metasurfaces (2D nanoantennas) have a limited probing volume near the plasma membrane. Inspired by high-aspect-ratio nanostructures, we demonstrate that integrating plasmonic metasurfaces with tall dielectric nanostructures significantly improves FTIR spectroscopy sensing capabilities.

## Summary of Research:

Infrared (IR) spectroscopy is widely employed to identify chemical compounds and has numerous biological applications. We developed Metasurface-Enhanced Infrared Spectroscopy (MEIRS) to measure live cell activity under physiological conditions. In MEIRS, cells are cultured on plasmonic nanoantenna arrays (metasurfaces) that enhance IR absorption. We have utilized MEIRS to detect changes in cell adhesion, cholesterol levels, and intracellular signaling [1,2]. This work improves on MEIRS by combining plasmonic metasurfaces with nano-topography to enhance FTIR sensitivity and pave the way for an optical platform to study cell-nanostructure interactions.

Figures 1(a) and 1(b) illustrate schematics of different device designs we fabricated. Figure 1(a) shows a nanoantenna array atop dielectric pillars (referred to as 3D nanoantennas), while Figure 1(b) displays an array of gratings atop dielectric pillars (referred to as 3D nanogratings). These high-aspect-ratio metasurfaces consist of gold nanoantennas on silica nanopillars deposited on IR-transparent CaF<sub>2</sub> substrates. The CaF<sub>2</sub> substrate is first cleaned using an oxygen plasma etcher (Anatech Resist Strip) and then coated with a 1 μm layer of SiO<sub>2</sub> using plasma-enhanced chemical vapor deposition (Oxford PECVD) to form the dielectric thin film. Metasurface patterns are defined using electron beam lithography with the JEOL 9500 system and poly(methyl methacrylate) (PMMA) as the resist. Layers of 5 nm Cr, 70 nm Au, and 20 nm Cr (as a hard mask for the subsequent etch step) are deposited using the SC4500 evaporator. If necessary, metasurfaces fabricated on large substrates (up to 4" diameter) are diced into smaller pieces using a DISCO dicing saw. The final step involves cleaning the metasurface sample with an oxygen plasma etcher (Anatech Resist Strip).

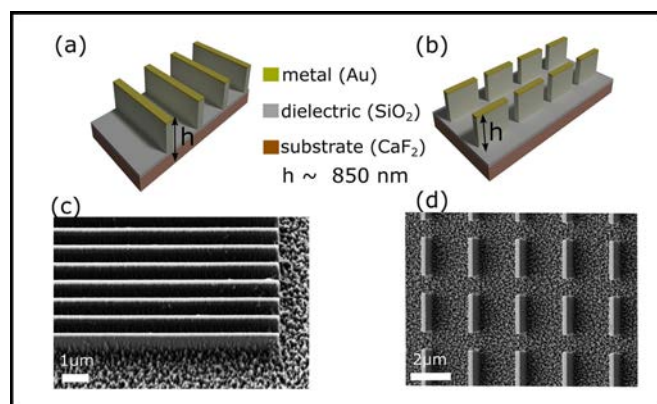


*Figure 1: High-aspect-ratio metal-on-dielectric metasurfaces. (a) and (b) show schematic of 3D nanograting device and 3D nanoantenna metasurface respectively. (c) and (d) are SEM images of the fabricated 3D nanograting device and 3D nanoantenna metasurface respectively (Scale bar: 1 μm and 2 μm, respectively).*

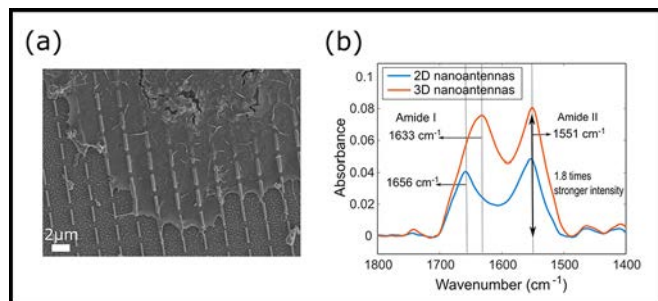


Figure 2: (a) SEM image of a human skin cancer cell on the 3D nanoantenna metasurface. (Scale bar: 2  $\mu\text{m}$ ) (b) Comparison of Fourier Transform Infrared Absorbance spectra of human skin cancer cells grown on 2D and 3D nanoantenna metasurfaces.

The metasurface is then attached to superstructures for cell culture chambers, and cells are grown on top of the metasurface for analysis. Figure 1(c) shows the fabricated 3D nanoantennas device, and Figure 1(d) depicts the fabricated 3D nanograting device.

When cells attach to high-aspect-ratio metasurfaces, they exhibit cellular responses not observed with flat 2D nanoantennas. One notable response is the induction of plasma membrane curvature, leading to cell deformation and wrapping around the vertical structures in accordance with the surface nanotopography. This phenomenon of cell wrapping addresses the issue of shallow field penetration seen with 2D metasurfaces, utilizing an optical process called transflection.

Figure 2(a) shows an SEM image of fixed and dried cells grown on these 3D nanoantennas. The nanoantennas, which are 1.8  $\mu\text{m}$  long, reflect light in the spectral region of 1500  $\text{cm}^{-1}$  to 1700  $\text{cm}^{-1}$ , suitable for analyzing proteins (amides) in cells. Figure 2(b) compares the infrared absorbance spectra obtained from cells grown on 2D and 3D nanoantenna metasurfaces. Spectra from the 3D nanoantenna metasurfaces (about 850 nm tall) exhibit a 1.8-fold improvement in spectral intensity in the Amide II region. A signature of unique cellular responses induced by the vertical nanostructures is also evident from the peak shift in the Amide I region observed in Figure 2(b).

While the 3D nanoantennas are resonant structures that reflect light only in specific spectral ranges based on antenna design, the 3D nanograting device shown in Figures 1(b) and 1(d) is a broadband optical device utilizing non-resonant plasmonic structures [3]. This device functions similarly to a wire grid polarizer under normal incidence, reflecting light with an electric field polarized parallel to the gratings when the

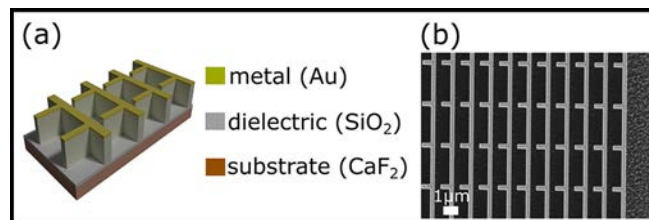


Figure 3: Grantenna — a device which can function as both 3D nanoantenna and 3D nanograting depending on the incident light polarization. (a) Schematic of device. (b) SEM image of fabricated device. (Scale bar: 1  $\mu\text{m}$ ).

grating periodicity is much smaller than the incident wavelength. This broadband reflectance device can be used for biological sensing of cells or other analytes in the region between the dielectric pillars. For the 3D nanoantennas, the plasmonic near fields are strongest near the gold nanoantenna, while for the 3D nanograting, the fields are strongest near the substrate (away from the gold layer) due to the standing wave effect. This makes the two devices complementary for studying live cells. The 3D nanoantennas are particularly sensitive to the cellular region around the metallic nanoantenna (the plasma membrane), whereas the 3D nanograting is more sensitive to the cell body in the trenches separating the tall dielectric gratings.

The device shown in Figure 3 combines the functionality of 3D nanoantennas and 3D nanograting into one, which we refer to as Grantennas. Depending on the polarization of the incident light, this device functions as either a 3D nanoantenna metasurface or a 3D nanograting. In the future, in addition to microwell-based cellular spectroscopy, we plan to employ these devices for rapid chemical imaging of live cells with sub-cellular resolution.

## References:

- [1] Huang, S. H., et al. Monitoring the effects of chemical stimuli on live cells with metasurface-enhanced infrared reflection spectroscopy. *Lab Chip* 21, 3991-4004 (2021).
- [2] Huang, S. H., et al. Metasurface-enhanced infrared spectroscopy in multiwell format for real-time assaying of live cells. *Lab Chip* 23, 2228-2240 (2023).
- [3] Mahalanabish, A.; Huang, S.; Shvets, G. Inverted Transflection Spectroscopy of Live Cells Using Metallic Grating on Elevated Nanopillars. *ACS Sens* 9 (3), 1218-1226 (2024).

# Biomimetic Loading Promotes Maturation and Suppresses Pathological Progression of Chick Embryonic Cardiomyocytes in Engineered Heart Tissues

**CNF Project Number: 2619-17**

**Principal Investigator(s): Jonathan T. Butcher**

**User(s): Mong Lung Steve Poon**

*Affiliation(s): Department of Biomedical Engineering, Cornell University*

*Primary Source(s) of Research Funding: Additional Ventures Single Ventricle Research Fund; National Institutes of Health R01 HL160028*

*Contact: jtb47@cornell.edu, mp773@cornell.edu*

*Research Group Website: <https://www.butcherlab.com/>*

*Primary CNF Tools Used: Objet30 pro 3D printer*

## Abstract:

Mechanical stimulation of engineered cardiac tissue was shown to improve cardiomyocyte maturation by emulating the mechanical loadings cardiomyocyte experienced during cardiac cycle, namely resistance to contraction (Afterload) and cyclic stretching (Preload). Nevertheless, many existing platforms for cyclic stretching pose the risk of inducing human cardiac pathology. In this study, we developed a novel bioreactor system to more accurately recapitulate the *in vivo* loading condition, allowing cyclic stretching with active contractile work production and duty cycling incorporated in between each stretch. Our focus was to investigate the functionalities, maturation, and pathological progression of embryonic chicken engineered heart tissues (EHTs) subjected to three distinct mechanical stimulation regimens, including (i) static control, (ii) afterload no duty cycle (Afterload NoDC), and (iii) afterload duty cycle (Afterload DC). We showed that Afterload DC improved tissue functionalities, maintaining higher contractile force and frequency. This was achieved by prohibiting early tissue compaction during stimulation. Tissues exposed to Afterload DC demonstrated enhanced cardiomyocyte maturation evidenced by improved sarcomeric organization.

Moreover, Afterload DC suppressed the transcriptional expressions of pathological hypertrophy and fibrosis markers, including TGF.2, COL5A2, and POSTN. Collectively, Afterload DC significantly promoted the functionality of EHTs by enhancing cardiomyocyte maturation and suppressing cardiac pathology. This study highlighted the remarkable potential of biomimetic loadings in facilitating tissue maturation.

## Summary of Research:

To determine if utilizing a mechanical stimulation regimen that can provide cyclic stretching while allowing contractile work production improves the tissue functionalities, contractile forces and frequencies of EHTs during auxotonic contraction were measured over seven days of stimulation (Figure 1). A

decline in contractile force was observed from D5 to D11 in all conditions (Figure 1A). However, both Afterload DC and Afterload NoDC groups had a general maintenance of the contractile force across culture time with a less degree of a decline. When comparing each condition, the afterload DC conditioned tissues showed a significantly greater force compared to the other conditions observed as early as the fifth day of stimulation. In terms of contractile frequency, Afterload NoDC and Afterload DC led to an increase in contractile frequency to a level significantly higher than that of the static control starting from D7 (Figure 1B). This incline in contractile frequency was shown to be followed by a mild decrease until D11 while most of the tissues in static control gradually lost their contraction.

To examine the effect of different mechanical stimulation regimens on tissue compaction, brightfield images of EHTs were taken over the culture period (Figure 2A). EHTs from all regimens exhibited spontaneous compaction in volume from D4 to D5 prior to the application of mechanical stimulation (Figure 2B). From D5, both Afterload NoDC and Afterload DC interrupted the compaction process, leading to significantly higher tissue volume of EHTs on D8 relative to those from the static control. This prohibiting effect was sustained until D11 only in Afterload NoDC, whereas EHTs subjected to Afterload DC showed a tissue volume similar to that of the static control. Our results showed that the percentage change of tissue volume from D5 to D8 was significantly and positively correlated with the percentage change of contractile force, in which afterload NoDC and afterload DC promote higher tissue volume and therefore higher contractile force (Figure 2C).

We investigated whether the improved tissue functionalities of EHTs following Afterload NoDC and Afterload DC conditioning is associated with enhanced cardiomyocyte maturation [1]. To do so, EHTs were stained with  $\alpha$ -Actinin to visualize the sarcomeric organization of cardiomyocytes (Figure 3A). As expected, tissues exposed to Afterload

NoDC and Afterload DC conditioning demonstrated more aligned sarcomere structure compared to those in the static control group. More importantly, both mechanical stimulation regimens led to sarcomere and z-band lengths resembling that of the mature chick cardiomyocytes.

Increasing afterload was shown to promote pathological hypertrophy and fibrosis despite improved tissue functionalities of EHTs. Here, EHTs subjected to Afterload NoDC condition were stretched while being prohibited from contractile work production by providing a consistently high afterload. To assess whether pathological phenotypes were manifested in the tissues under Afterload NoDC and whether Afterload DC can mitigate the pathological progression, smFISH staining was performed on a panel of gene markers associated with pathological hypertrophy and cardiac fibrosis (Figure 4). Aligned with previous study, tissues in the Afterload NoDC group showed significantly higher expression of pathological hypertrophy markers, including POSTN, TGF.2, and COL5A2, compared to the static control. Surprisingly, despite being exposed to mechanical loading, EHTs in the Afterload DC condition showed similar marker expression to the static control. No significant difference among conditions was detected in FN1 expression.

### Conclusion and Future Steps:

Our study highlights the promising potential of Afterload DC in promoting EHTs functionality by promoting cardiomyocyte maturation while preventing pathological phenotypes. To expand, assessing the effect of biomimetic loading on human induced pluripotent stem cell-derived cardiomyocyte will greatly facilitate the clinical translation of this novel mechanical stimulation regimen. Meanwhile, our bioreactor system could also serve as a platform for drug screening and disease modeling.

### References:

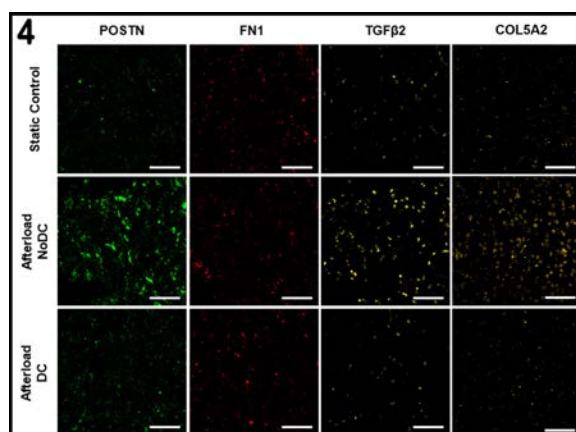
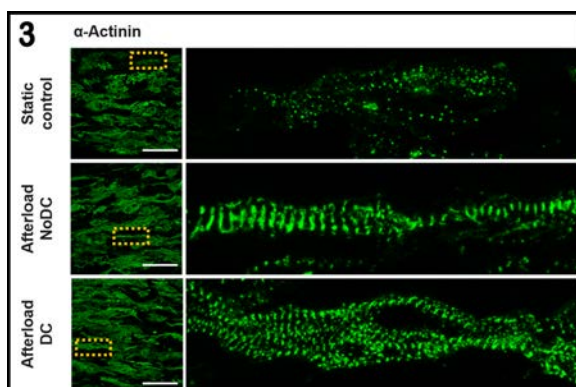
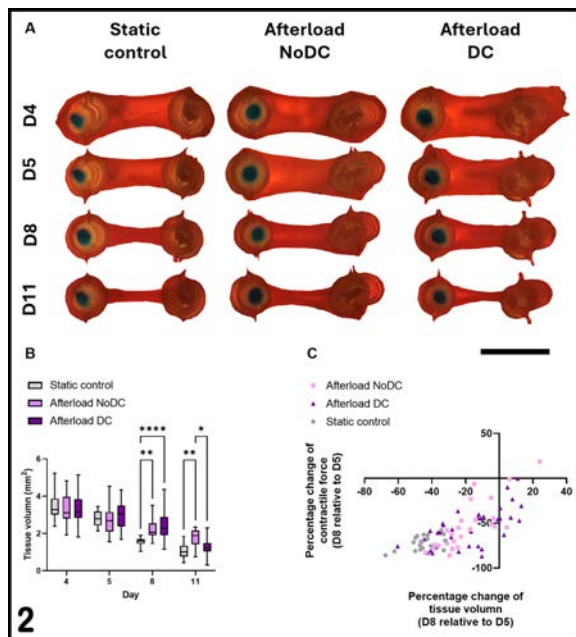
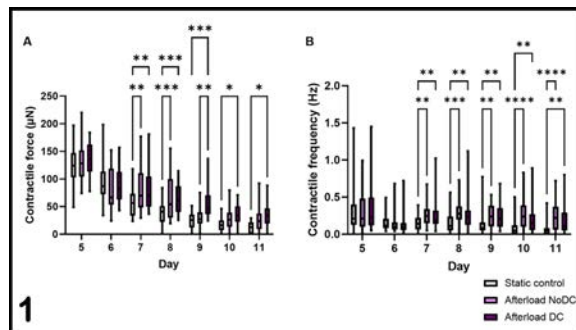
[1] Leonard, Andrea, et al. "Afterload promotes maturation of human induced pluripotent stem cell derived cardiomyocytes in engineered heart tissues." *Journal of molecular and cellular cardiology* 118 (2018): 147-158.

Figure 1: Auxotonic contractile capacity of EHTs on post constructs across stimulation period. Contractile force (A) and frequency (B) across culture time for all three stimulation conditions.

Figure 2: Compaction of EHTs on post construct across stimulation period. (A) Bright field images of EHTs across culture time for all three stimulation conditions. (B) Quantitative measurement of tissue volume of EHTs across culture time. (C) Correlation between percentage change of contractile force and percentage change of tissue volume from D5 to D8 and D8 to D11.

Figure 3: Cardiomyocyte maturation in EHTs on Day 11. (A) Representative immunofluorescent images of  $\alpha$ -actinin. Quantitative measurement of the sarcomere length (B) and the z-band length

Figure 4: Expression of gene markers associated with fibrosis and pathological hypertrophy in EHTs on Day 11.



## Micro-Scale Optoelectronic Transduced Electrodes (MOTEs) for Chronic *in vivo* Neural Recording

**CNF Project Number(s): 2657-18, 2836-19**

**Principal Investigator(s): Prof. Alyosha C. Molnar**

**User(s): Sunwoo Lee, Shahab Ghajari, Sanaz Sadeghi, Devesh Khilwani**

*Affiliation(s): Electrical and Computer Engineering, Cornell University*

*Primary Source(s) of Research Funding: National Institute of Health*

*Contact: am699@cornell.edu, sl933@cornell.edu, sg2367@cornell.edu, ss3842@cornell.edu, dk842@cornell.edu*

*Research Group Website: <https://molnargroup.ece.cornell.edu/>*

*Primary CNF Tools Used: ABM Contact Aligner, AJA Sputter, and Westbond 7400A Ultrasonic Wire Bonder, Oxford 100/81/82, UNAXIS Deep Si Etcher, Oxford PECVD/ALD, Anatech, P7 Profilometer, Zeiss SEMs*

### Abstract:

Elucidating how the brain functions requires chronic *in vivo* recording of neural activity in live animals. However, existing neural recording technologies have thus far failed to provide a tetherless and fully implantable neural recording unit that can function chronically. Instead, existing techniques typically require electrodes to be tethered to the outside world directly via a wire, or indirectly via an RF Coil [1], which is much larger than the electrodes themselves, causing irrevocable damages associated with the residual motions between electrodes and neurons as the brain moves. On the other hand, optical techniques, which are becoming increasingly popular, are often limited to subsets of neurons in any given organism, impeded by scattering of the excitation light and emitted fluorescence, and limited to low temporal resolution [2]. Here we heterogeneously integrate III-V optical devices on complementary metal-oxide-semiconductor (CMOS) via a layer transfer, creating Micro-scale Optoelectronic Transduced Electrodes (MOTEs), which are powered by and are communicating optically, combining many benefits of optical techniques with high temporal-resolution of electrical recording. Our work not only represents the smallest neural recorder to date but is also the first to be demonstrated to be functional *in vivo* and chronically (> 5 months) in awake mice.

### Summary of Research:

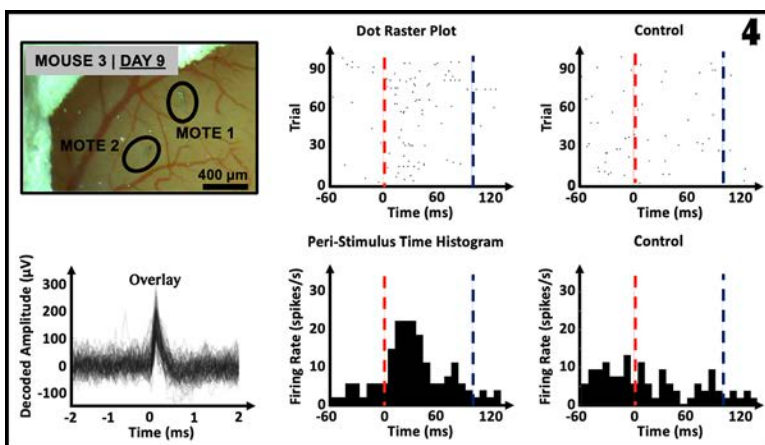
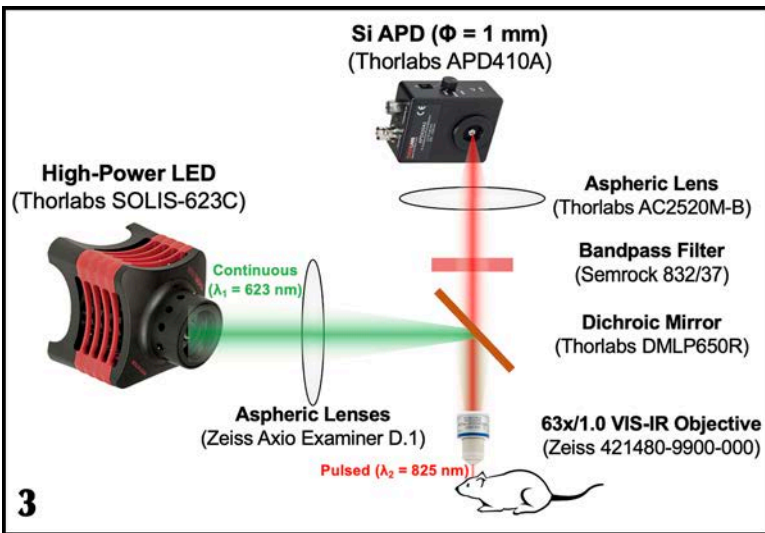
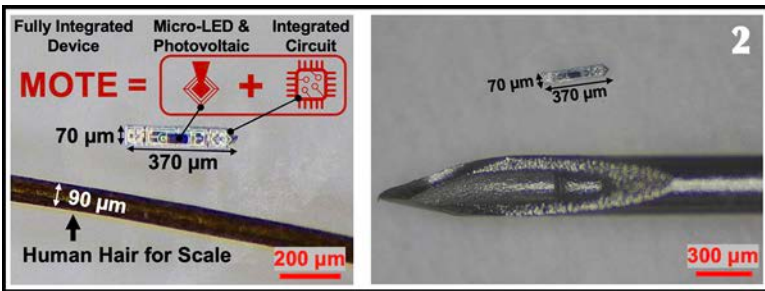
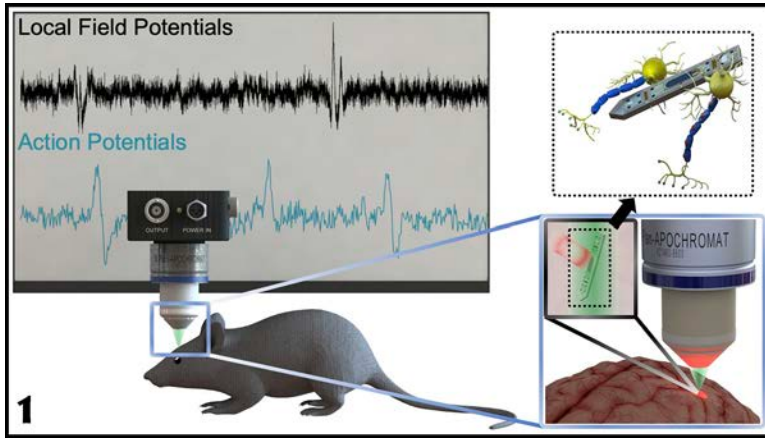
Our fabrication starts with about 5 mm x 5 mm, conventional 180 nm CMOS die, which contains the electronics for signal amplification, encoding, and transmission [3,4]. The CMOS die is then integrated with AlGaAs diode which acts as a photo-voltaic (PV) as well as light emitting diode (LED), hence the diode is abbreviated as PVLED [5]. The PVLED provides an optical link which powers the electronics and transmits

encoded signals in optical pulses. The MOTE utilizes Pulse Position Modulation (PPM) for signal encoding for its high information-per-photon efficiency, where the spacing between the output pulses is proportional to the measured electric field of neuronal signals across the measurement electrodes. Figure 1 depicts a conceptual deployment and system description of such MOTE, whereas Figure 2 shows the impressive scaling enabled through the MOTE's heterogeneous integration (< 1 nanoliter in volume and ~1 µg in weight).

The MOTEs are completely untethered, hence free of any detrimental relative motion often observed in tethered or wired neural recording units. Instead, the MOTEs are powered optically, and through the PPM, emits the measured neural signals optically as well, at a longer wavelength than the “powering” wavelength. Figure 3 illustrates the measurement setup associated with the MOTEs where a 623 nm LED was used to power the MOTE, which in turn emits the PPM pulses that encode the neural activities at the 825 nm wavelength. The MOTEs have been implanted in mouse brains, and we were able to measure the neural activities chronically for more than 5 months (and counting), during which time the foreign body response seemed to be minimal thanks to their miniscule size, and the neural signals were quite stable. Figure 4 provides example measurements of action potential spikes from one such mouse brain where the MOTEs were embedded in its barrel cortex so that the recording can be done in a cause-and-effect fashion (i.e., a touch whisker activating barrel cortex responses).

### Conclusions and Future Steps:

A MOTE is the smallest electrophysiological sensor of its kind, enabled through an ingenious heterogeneous integration approach that leverages multiple disciplines:



electronics, optics, nano/microfabrication, and electrophysiology. The next step would entail not only improving the circuits and the devices of the MOTEs but paving the path toward the mass production so to provide interested biolaboratories the MOTEs samples, and to examine the commercial viability. In parallel, applying existing MOTEs to biological studies previously unapproachable such as chronic in-organoid measurements is our near term goal.

## References:

- [1] R. R. Harrison, et al., "A Low-Power Integrated Circuit for a Wireless 100-Electrode Neural Recording System," *IEEE J. Solid-State Circuits*, vol. 42, no. 1, pp. 123-133, Jan. 2007, doi: 10.1109/JSSC.2006.886567.
- [2] W. Yang and R. Yuste, "In vivo imaging of neural activity," *Nat Methods*, vol. 14, no. 4, Art. no. 4, Apr. 2017, doi: 10.1038/nmeth.4230.
- [3] S. Lee, A. J. Cortese, P. Trexel, E. R. Agger, P. L. McEuen, and A. C. Molnar, "A 330 μm x 90 μm opto-electronically integrated wireless system-on-chip for recording of neural activities," in *2018 IEEE International Solid-State Circuits Conference (ISSCC)*, Feb. 2018, pp. 292-294. doi: 10.1109/ISSCC.2018.8310299.
- [4] S. Lee, A. J. Cortese, A. P. Gandhi, E. R. Agger, P. L. McEuen, and A. C. Molnar, "A 250 μm x 57 μm Microscale Opto-electronically Transduced Electrodes (MOTEs) for Neural Recording," *IEEE Transactions on Biomedical Circuits and Systems*, vol. 12, no. 6, pp. 1256-1266, Dec. 2018, doi: 10.1109/TBCAS.2018.2876069.
- [5] S. Lee, et al., "Fabrication of Injectable Micro-Scale Opto-Electronically Transduced Electrodes (MOTEs) for Physiological Monitoring," *J. Microelectromech. Syst.*, vol. 29, no. 5, pp. 720-726, Oct. 2020, doi: 10.1109/JMEMS.2020.2999496.

Figure 1: System level description of the micro-scale optoelectronic transduced electrodes (MOTEs) in a mouse brain.

Figure 2: Fully fabricated MOTEs next to S. Lee's hair (left) and a 31-gauge insulin needle (right).

Figure 3: Schematic of the MOTE-based measurement system, which the MOTE is powered and is communicating optically.

Figure 4: In vivo neural recording demonstrating that the MOTEs are indeed able to measure neural activities such as action potentials chronically.

# On-Chip Cell Transportation and Rotation Using Vibration-Induced Flow

**CNF Project Number: 2827-19**

**Principal Investigator(s): Alireza Abbaspourrad**

**User(s): Amirhossein Favakeh, Amir Mokhtare**

*Affiliation(s): Department of Food Science, Cornell University*

*Primary Source(s) of Research Funding: Ignite: Cornell Research Lab to Market, Center for Technology Licensing*

*Contact: alireza@cornell.edu, af446@cornell.edu, am2964@cornell.edu*

*Research Group Website: <https://abbaspourradlab.com/>*

*Primary CNF Tools Used: ABM Contact Aligner, Heidelberg Mask Writer - DWL2000, Dicing Saw - DISCO, P7 Profilometer*

## Abstract:

We present a system for cell manipulation based on vibration-induced flow (VIF), the science of acoustic streaming generated around the microstructure on a chip using circular vibration. This technique is easy to handle and applicable to an open-surface chip structure. It is a simple method involving a chip on an XY piezoelectric stage and is known for its simplicity. Thus, large cells can be manipulated by the applied flow velocity in the order of 100  $\mu\text{m/s}$  close to the micropillar arrays. We designed the micropillar array to control the mouse oocytes' transportation, rotation, and manipulation. The induced flow around the micropillars can be controlled by the applied frequency, amplitude, and shape/arrangement of the micropillar structure.

## Summary of Research:

Recent advances in micro/nanofabrication and microfluidics have improved the manipulation of small biological objects, such as cells or microorganisms [1]. We present a transportation method based on vibration-induced flow (VIF) to move the mouse oocytes through the micropillar arrays on the open surface chip [2]. This chip is a candidate for being simple, low-cost, and easy to use, while offering accessible (open-structured) microfluidic channels for cell pickup. As shown in Figure 1, we fabricated the micropillars with a one-step photolithography process. First, SU-8 100 was poured on a fused silica wafer with a thickness of 500  $\mu\text{m}$  and spun at 1500 rpm for 30 seconds. Next, the wafer was baked for 25 minutes at 65°C and for 70 minutes at 95°C. Then we exposed the baked wafer to UV light for

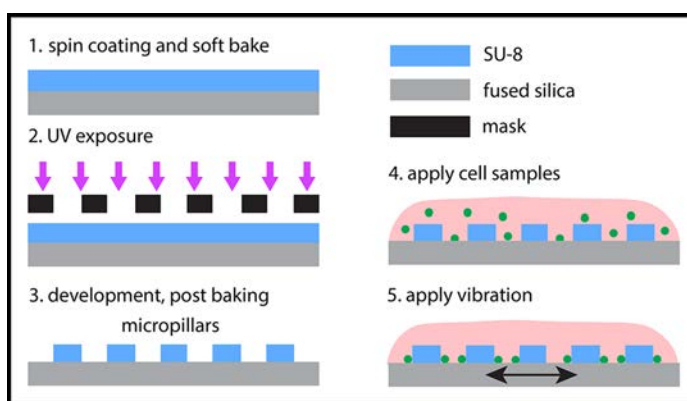


Figure 1: Schematic of fabrication process and experiment procedure.

one minute with an ABM contact aligner, followed by post-exposure baking at 95°C for 20 minutes. Finally, we submerged the wafer in SU-8 developer for 17 minutes before hard baking. The pillars' thickness was 200  $\mu\text{m}$ , as measured by P7 Profilometer. Subsequently, the chips were separated using Dicing Saw DISCO, and a photograph of one of the chips is shown in Figure 2a. We fixed the chip on the XY piezoelectric stage. We generated the circular vibration with two sinusoidal wave signals with 90° offset in phase to the piezo driver via the waveform generator. The applied frequency and voltage were 200 Hz and 1 V, respectively. A culture medium containing mouse oocytes was directly dropped onto the chip (Figure 2b).

Figure 2c shows the concept of transporting and trapping cells into the center of the chip. By applying a circular vibration, a whirling flow is induced around each pillar, and since the pillars' pitch is designed to interfere with each other, a whirling flow is induced through the micropillar array. Since this system has enough power to generate fluid force to manipulate large cells, we can move the cells to any desired destination by adjusting the micropillar array and the distance between each pillar. For example, we fabricated the arrays in a spiral pattern to gather the mouse oocyte cells to the center of the chip. As a result, this technique can be utilized for flow control and cell transportation on an open-surface chip for any type of cell.

### Conclusion:

We experimentally investigated the effect of VIF on mouse oocyte transportation and manipulation. Cells can be extracted easily since the chip has easy access to an external environment. Therefore, an operator can detect the cells with their eyes, collecting them with microinjectors, and there is no worry of losing the cells on the chip.

### References:

- [1] Reyes, D. R., Iossifidis, D., Auroux, P.-A. & Manz, A. Micro total analysis systems. 1. Introduction, theory, and technology. *Anal. Chem.* 74, 2623-2636 (2002).
- [2] Hayakawa, T., Sakuma, S. & Arai, F. On-chip 3D rotation of oocyte based on a vibration-induced local whirling flow. *Microsystems & Nanoengineering* 1, 1-9 (2015).

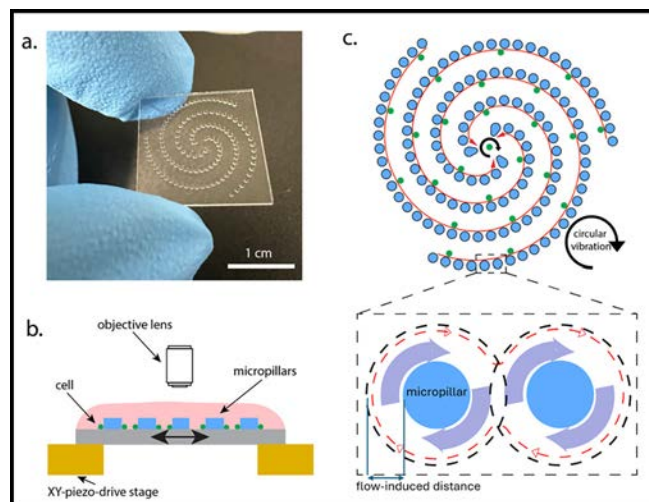


Figure 2: a. Photograph of the fabricated chip. b. Schematic of experimental setup. c. Concept of cell transportation using vibration-induced flow.

## Fabrication of Microchip Devices for Organ-on-a-Chip and Lab-on-a-Chip Applications

**CNF Project Number: 2857-19**

**Principal Investigator(s): Esak (Isaac) Lee, Ph.D.**

**User(s): Renhao Lu, Yansong Peng, Shufan Yin**

*Affiliation(s): Meinig School of Biomedical Engineering, Cornell University*

*Primary Source(s) of Research Funding: National Institutes of Health (NIH) R01 HL165135 and R01 CA279560*

*Contact: el767@cornell.edu, rl839@cornell.edu, yp255@cornell.edu, sy766@cornell.edu*

*Research Group Website: <https://leelab.bme.cornell.edu/>*

*Primary CNF Tools Used: Heidelberg Mask Writer DWL2000, ABM Contact Aligner, MVD100*

### Abstract:

Organ-on-a-chip is a microfluidic cell culture platform, integrated circuit (chip) that simulates the activities, mechanics, and physiological response of an entire organ or an organ system. Our lab aims to create organ-on-a-chip devices to study the mechanism of various diseases. In the past year, we mainly focused on two projects: (1) A 3D biomimetic model of lymphatics reveals cell–cell junction tightening and lymphedema via a cytokine-induced ROCK2/JAM-A complex; (2) Piezo1 regulates meningeal lymphatic vessel drainage and alleviates excessive CSF accumulation.

### Summary of Research:

#### **Project 1: A 3D biomimetic model of lymphatics reveals cell–cell junction tightening and lymphedema via a cytokine-induced ROCK2/JAM-A complex [1].**

Impaired lymphatic drainage and lymphedema are major morbidities whose mechanisms have remained obscure. To study lymphatic drainage and its impairment, we engineered a microfluidic culture model of lymphatic vessels draining interstitial fluid. This lymphatic drainage-on-chip revealed that inflammatory cytokines that are known to disrupt blood vessel junctions instead tightened lymphatic cell–cell junctions and impeded lymphatic drainage. This opposing response was further demonstrated when inhibition of rho-associated protein kinase (ROCK) was found to normalize fluid drainage under cytokine challenge by simultaneously loosening lymphatic junctions and tightening blood vessel junctions. Studies also revealed a previously undescribed shift in ROCK isoforms in lymphatic endothelial cells, wherein a ROCK2/junctional adhesion molecule-A (JAM-A) complex emerges that is responsible for the cytokine-induced lymphatic junction zippering. To validate these in vitro findings, we further demonstrated in a genetic

mouse model that lymphatic-specific knockout of ROCK2 reversed lymphedema in vivo. These studies provide a unique platform to generate interstitial fluid pressure and measure the drainage of interstitial fluid into lymphatics and reveal a previously unappreciated ROCK2-mediated mechanism in regulating lymphatic drainage.

#### **Project 2: Piezo1 regulates meningeal lymphatic vessel drainage and alleviates excessive CSF accumulation [2]**

Piezo1 regulates multiple aspects of the vascular system by converting mechanical signals generated by fluid flow into biological processes. In this project, we utilize the lymphatic-on-chip devices to study the role of Piezo1 in lymphatics and its drainage functions. Together with our collaborators, we find that Piezo1 is necessary for the proper development and function of meningeal lymphatic vessels and that activating Piezo1 through transgenic overexpression or treatment with the chemical agonist Yoda1 is sufficient to increase cerebrospinal fluid (CSF) outflow by improving lymphatic absorption and transport. The abnormal accumulation of CSF, which often leads to hydrocephalus and ventriculomegaly, currently lacks effective treatments. We discovered that meningeal lymphatics in mouse models of Down syndrome were incompletely developed and abnormally formed. Selective overexpression of Piezo1 in lymphatics or systemic administration of Yoda1 in mice with hydrocephalus or Down syndrome resulted in a notable decrease in pathological CSF accumulation, ventricular enlargement and other associated disease symptoms. Together, our study highlights the importance of Piezo1-mediated lymphatic mechanotransduction in maintaining brain fluid drainage and identifies Piezo1 as a promising therapeutic target for treating excessive CSF accumulation and ventricular enlargement.

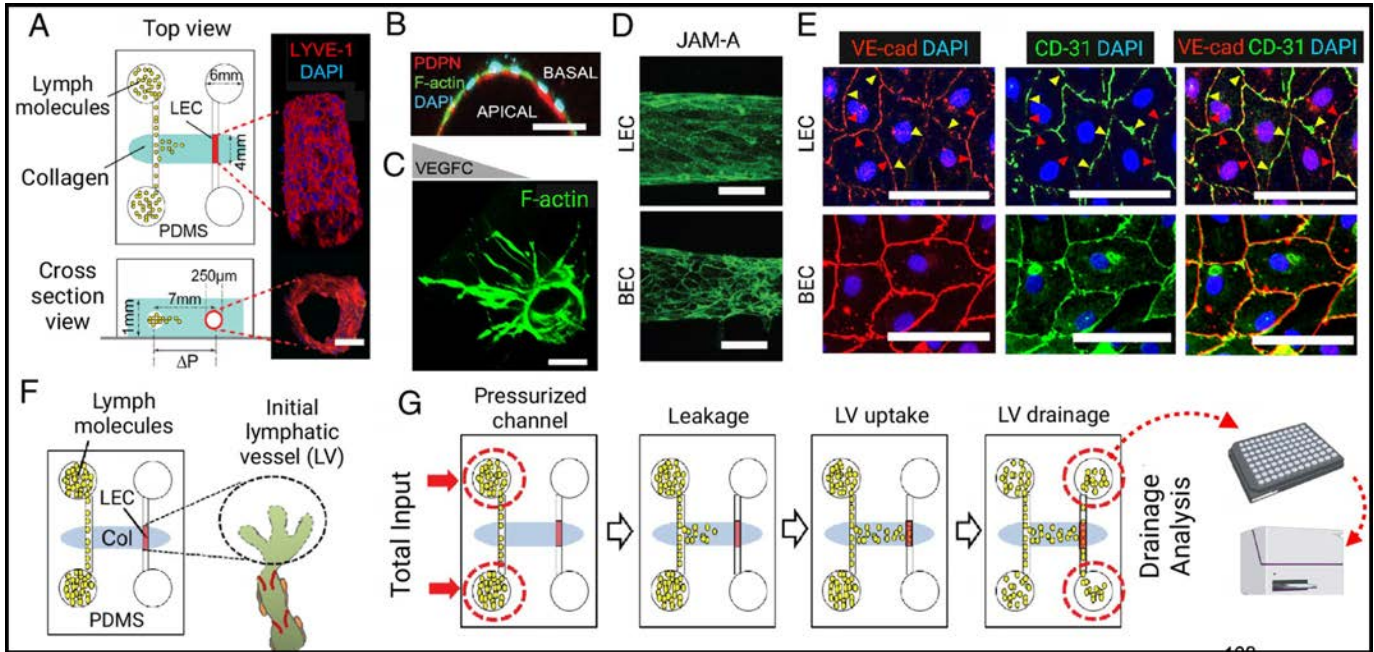


Figure 1, above: Lymphatic drainage-on-chip recapitulates lymphatic structure, drainage, and dysfunction. (A) A schematic of the lymphatic drainage-on-chip platform. (B) Apical podoplanin (PDPN) expression on the luminal side of the vessel. (C) Lymphatic sprouting in response to VEGFC stimulation. (D) Immunostaining of LEC-generated lymphatic vessels and BEC-generated blood vessels with a tight junction marker, JAM-A. (E) Immunostaining of lymphatic vessels and blood vessels with an adherens junction marker, VE-cadherin (VE-cad), and CD31. Red and yellow arrows indicate exclusive expression of VE-cad and CD31, respectively, showing interdigitated, discontinuous expression of VE-cad in LECs. (F) A schematic of a biomimetic lymphatic drainage-on-chip model system. The engineered lymphatic vessel (LV) in the right-side channel functions as an initial LV to drain interstitial lymph fluid that is introduced through the left-side channel. (G) Transport of lymph fluid. The left-side channel pressured with lymph fluid induces fluid transport. The pressure gradient between two channels results in fluid convection from the left channel to the engineered LV. The lymph fluid is drained by the engineered LV and accumulated in two right-side reservoirs. Total drained fluid is analyzed to obtain the number of drained lymph molecules.

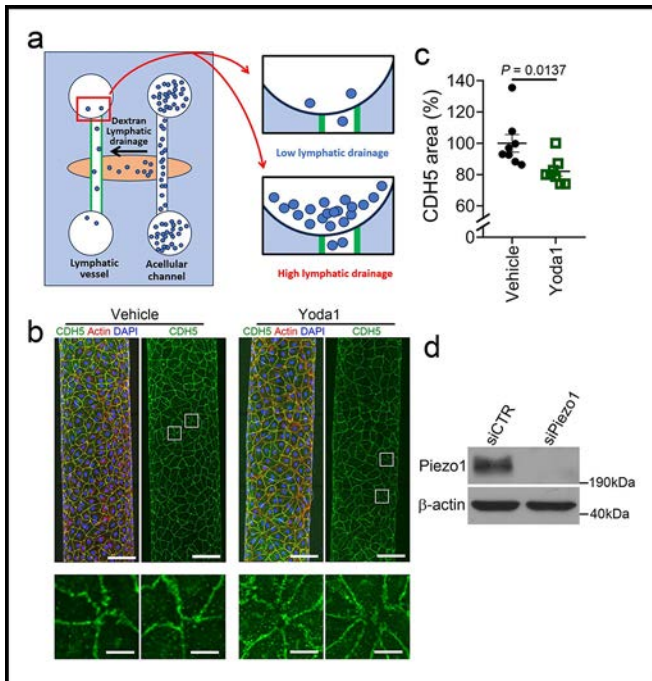


Figure 2, left: (a) Schematic illustration of the 3-D lymphatic vessel model used for this study. The outcome of the Yoda1-induced drainage increase is presented in Fig. 4c. (b) Fluorescence confocal images of the engineered lymphatic vessels stained for F-actin and CDH5. Enlarged CDH5 images (boxed) show more discontinuous junctions in the Yoda1-treated group than in the vehicle group. Scale bars: 100 .m (10 .m, enlarged images). Acellular channels are not shown. (c) The relative area of CDH5-stained cellular junctions (n.=.8 independent experiments). Statistics: two-tailed t-test. (d) Western blot assays verifying the efficient knock-down of Piezo1 in LECs prepared for the drainage measurement shown in Figure 4c (n.=.4 independent samples). Data are presented as mean values +/- SEM.

References:

[1] Lee E, et al. A 3D biomimetic model of lymphatics reveals cell-cell junction tightening and lymphedema via a cytokine-induced ROCK2/JAM-A complex. Proc Natl Acad Sci U S A. 2023 Oct 10;120(41):e2308941120. doi: 10.1073/pnas.2308941120. Epub 2023 Oct 2. PMID: 37782785; PMCID: PMC10576061.

[2] Choi D, et al. Piezo1 regulates meningeal lymphatic vessel drainage and alleviates excessive CSF accumulation. Nat Neurosci. 2024 May;27(5):913-926. doi: 10.1038/s41593-024-01604-8. Epub 2024 Mar 25. PMID: 38528202; PMCID: PMC11088999.

# Investigating the Effect of the Tumor Microenvironment on Metastatic Progression Using Micro and Nano-Scale Tools

**CNF Project Number: 2912-20**

**CNF Principal Investigator(s): Claudia Fischbach<sup>1</sup>**

**User(s): Nicole Sempertegui<sup>1</sup>, Garrett Beeghly<sup>1</sup>, Jack Crowley<sup>2</sup>**

*Affiliation(s): 1. Biomedical Engineering, 2. Applied and Engineering Physics; Cornell University*

*Primary Source(s) of Research Funding: Breast Cancer Coalition of Rochester Trainee Grant,*

*Center on the Physics of Cancer Metabolism Award Number 1U54CA210184-01, National Cancer Institute*

*Contact: cf99@cornell.edu, nds68@cornell.edu*

*Primary CNF Tools Used: ABM Contact Aligner, Heidelberg DWL2000, Hamatech 9000, Malvern NS300 NanoSight*

## Abstract:

Breast cancer is the second leading cause of cancer-related death for women in the United States [1]. Breast cancer mortality is driven by metastasis, where cancer cells disseminate from the primary tumor to seed distant tissues such as the bone. During bone metastatic disease, cancer cells interact with their microenvironment consisting of a mineralized, collagen-rich extracellular matrix and other cell types including mesenchymal stem cells (MSCs), macrophages, and osteoclasts. These cells are known to participate in reciprocal signaling with cancer cells to influence tumorigenesis through the exchange of soluble factors [2,3] and extracellular vesicles (EV). However, the mechanisms by which soluble factor and EV signaling influence tumor cell invasion and the development of a pro-tumorigenic microenvironment remain unclear due to the lack of models that enable systematic study. To this end, CNF tools were used to investigate various stages in metastasis: EV-mediated formation of a pre-metastatic niche in bone and tumor cell invasion into bone. For pre-metastatic niche development studies, we leveraged EVs derived from breast cancer cells and bone-mimetic engineered substrates to investigate how EV binding to bone is regulated by components of their glycocalyx (sugar-coating on the outside of EVs) and matrix mineral content. For invasion studies into the bone, we developed a microfluidic model of the bone microenvironment with mineralized collagen microchannels and have shown that tumor cell invasion is inhibited when co-cultured with macrophages and osteoclasts seeded in a mineralized microchannel.

## Summary of Research:

**Isolation of Breast Cancer-Derived Extracellular Vesicles and Interactions with Bone Matrix.** Prior to arriving at distant metastatic sites, tumor cells can release soluble factors and extracellular vesicles (EVs)

into circulation to prime the microenvironment of distant target organs for subsequent development of organotropic metastasis. EVs are gaining appreciation as stable vehicles of cell-derived cargo contributing to tumorigenesis and pre-metastatic niche (PMN) formation. In collaboration with Matt Paszek's Lab, we have successfully isolated and characterized EVs from murine 4T1s breast cancer cells using the Malvern NS300 NanoSight. Currently, we are investigating differences in 4T1 EV binding to bone-mimetic engineered substrates. These bone-mimetic models were developed at the CNF using SU-8 photolithography to create a micropatterned silicon wafer used to fabricate PDMS "microwells". These PDMS microwells are filled with a collagen type I matrix and subsequently mineralized using the polymer-induced liquid precursor (PILP) method to mimic bone extracellular matrix, as previously described [5]. Through this engineered system, we can systematically explore differences in EVs binding in the presence or absence of mineral in bone. Furthermore, we are examining how EV characteristics, such as glycocalyx composition, will affect binding to bone and whether this is dependent on matrix mineral content. Our preliminary data suggest that EV binding is increased in mineralized collagen substrates, and that removal of mucins from the glycocalyx reduces their ability to bind (Figure 1). Future work will incorporate MSCs in addition to EVs to probe the interplay between bone-resident cells, bone matrix and EVs. Overall, these studies will help unravel the mechanisms by which EVs and key components of the bone microenvironment regulate the onset of bone metastasis.

**Effects of Mineralized Collagen on Breast Cancer Cell Invasion Using a Microfluidic Model of the Bone.** During bone metastasis, tumor cell invasion and subsequent seeding of osteogenic niches [4] can be influenced by macrophages. Macrophages not only exert immunomodulatory effects, but also have the

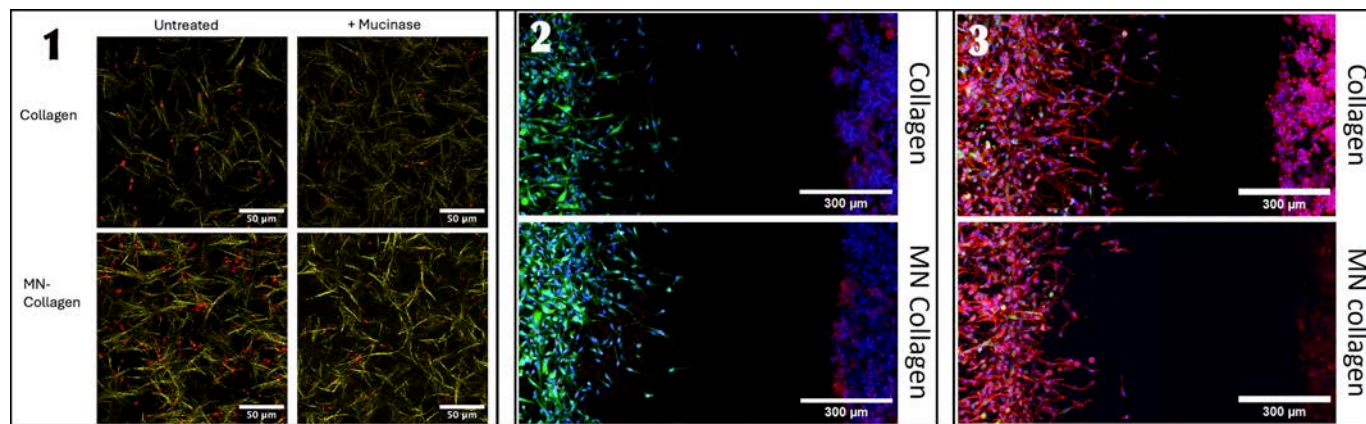


Figure 1, left: Confocal microscopy projection of 4T1 extracellular vesicles (EVs) stained with DiI lipophilic dye (red) in mineralized-collagen or collagen control microwells. Confocal reflectance was used to visualize collagen fibers (yellow). Scale bar: 50  $\mu\text{m}$ .

Figure 2, middle: Fluorescent microscopy of non-mineralized collagen device (top) and mineralized (MN) collagen device (bottom) seeded with MDA-MB-231 breast cancer cells (green) and RAW264.7 macrophages (red). DAPI was used to stain nuclei (blue) Scale bar: 300  $\mu\text{m}$ .

Figure 3, right: Fluorescent microscopy of non-mineralized collagen device (top) and mineralized (MN) collagen device (bottom) seeded with MDA-MB-231 breast cancer cells (green) and RAW264.7 osteoclasts. F-actin and nuclei are shown in red and blue, respectively. Scale bar: 300  $\mu\text{m}$ .

potential to differentiate into osteoclasts, the primary cell type driving osteolysis in bone metastasis patients. Using SU-8 photolithography in conjunction with the ABM Contact Aligner and a photomask generated by the Heidelberg DWL2000, we have created a dual channel microfluidic devices that enables co-culture breast cancer cells and macrophages encapsulated in a 3D collagen matrix. To model these interactions within a bone-like microenvironment, the microfluidic device was modified using the PILP method to include selective and controlled collagen mineralization of the device microchannels [5]. We have shown that macrophages promote the invasion of breast cancer cells regardless of collagen mineralization and that this effect occurs without cell-cell contact, suggesting that it was caused by soluble factors secreted from macrophages. However, it was determined that collagen mineralization inhibits the ability of macrophages to promote tumor cell invasion compared to non-mineralized collagen co-culture conditions (Figure 2). Similarly, when macrophages were differentiated into osteoclasts within a mineralized collagen channel, tumor cell invasion was also inhibited compared to non-mineralized collagen devices (Figure 3). Future work includes device materials characterization and validating our findings by incorporating syngeneic breast cancer cells with primary macrophages and osteoclasts.

### Funding Acknowledgements:

Breast Cancer Coalition of Rochester Trainee Grant (Nicole). The work described was supported by the Center on the Physics of Cancer Metabolism through Award Number 1U54CA210184-01 from the National Cancer Institute. The content is solely the responsibility of the authors and does not necessarily represent the official views of the National Cancer Institute or the National Institutes of Health.

### References:

- [1] Siegel, R. L., et al. Cancer Statistics, 2021. *CA. Cancer J. Clin.* 71, 7-33 (2021).
- [2] Tan, M. L., et. al. Engineering strategies to capture the biological and biophysical tumor microenvironment in vitro. *Adv. Drug Deliv. Rev.* 176, 113852 (2021).
- [3] Zheng, P., and Li, W. Crosstalk Between Mesenchymal Stromal Cells and Tumor Associated Macrophages in Gastric Cancer. *Front. Oncol.* 10, 1-9 (2020).
- [4] Peinado, H., et al. Pre-metastatic niches: organ-specific homes for metastases. *Nat. Rev. Cancer* 17, 302-317 (2017).
- [5] Choi, S., et al. Intrafibrillar, bone-mimetic collagen mineralization regulates breast cancer cell adhesion and migration. *Biomaterials.* 198, 95-106 (2019).

## Increasing Microfabrication Yield of Template-Based Carbon Nanotube Arrays for Gene Transfer

**CNF Project Number: 3106-23**

**Principal Investigator(s): Michael Schrlau**

**User(s): Mujtaba Y.K. Siddiqui**

*Affiliation(s): Department of Mechanical Engineering, Kate Gleason College of Engineering;  
Rochester Institute of Technology*

*Primary Source(s) of Research Funding: New York State Fuzehub*

*Contact: mgseme@rit.edu, mys8553@rit.edu*

*Research Group Website: <https://people.rit.edu/mgseme/Site/Home.html>*

*Primary CNF Tools Used: AJA Ion Mill, PT 740 RIE, KLA P7 Profilometer, GCA AS200 i-line Stepper, OXFORD 81 RIE*

### Abstract:

Carbon nanotube (CNT) arrays template-based fabricated biomedical devices used for gene transfer, they can be used to transport novel gene therapies into cells which help combat illnesses such as HIV and some types of cancers. These devices are a more economical and efficient alternative for delivery of gene therapies as compared to conventional methods [1]. The Cornell NanoScale Facility (CNF) offers tools used to fabricate these devices, research conducted there has increased production yield and reduced production time.

### Summary of Research:

CNT arrays produced using template-based fabrication have been shown in previous studies to possess the capability of supporting gene transfer. They have been reported to achieve 85% of plasmid DNA transfer into cells and show a three times higher efficiency for transfection in stem cells than standard lipofection methods [2]. Carbon nanotubes are produced on Anodic Aluminum Oxide (AAO) templates using a multistep fabrication process which involves cleanroom fabrication.

Etching tools at the CNF were utilized to create free standing tubes, Figure 1 shows Scanning Electron Micrograph (SEM) image of a CNT array device produced at CNF. The micrograph shows carbon tubes protruding from the surface of AAO, these tubes stand approximately 200 nm off the surface of the AAO substrate.

Commercially available AAO templates consist of self-aligned pores covered by an interconnected later of AAO creating a 'lattice'-like web of material that inhibits biomolecule transfer by creating a bottleneck —

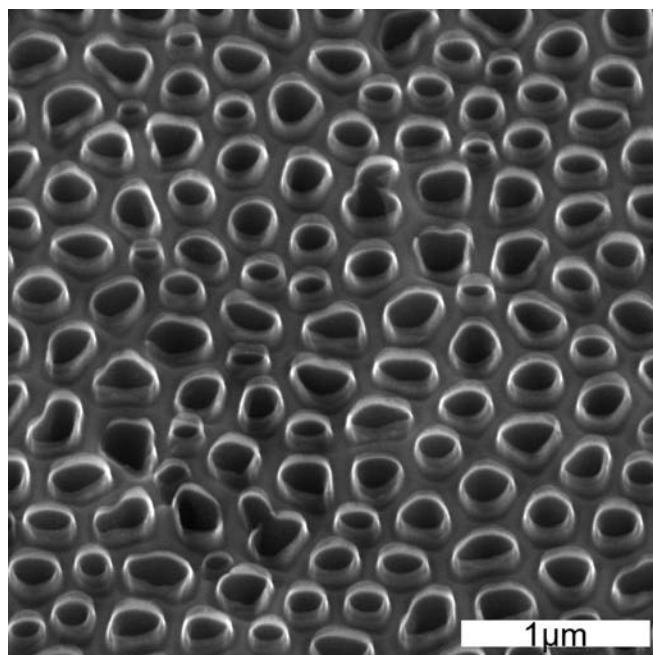


Figure 1: SEM of fabricated CNT.

this is referred as a lattice layer; during the fabrication of CNT arrays this layer needs to be removed, due to the size constraints and limitations of mechanical methods ion milling using the AJA ion mill at CNF was utilized to remove the top 1  $\mu\text{m}$  of the AAO, exposing the pores.

Figure 2 shows a schematic visualizing from a side view the effects of ion milling on the AAO template, we noticed etch depth correlates to visible hydraulic pore diameter. The figure shows the AAO being etched away over time removing the lattice layer at the top to reveal the wider pores underneath. Ion mill time was

optimized 1hr after it was noted that the pore diameter at both times were reported to be statistically similar. This was reconfirmed by various repeats before being implemented into the standard procedure used to fabricate CNT arrays.

The devices are 13 mm disks with a thickness of 60  $\mu\text{m}$ , these pieces are too small to fit into the CNF tools which are built to work with 4" and 6" wafers. A carrier wafer was designed and produced to hold multiple CNT arrays to increase production yield up to 60 devices at a time. Figure 3 shows a carrier wafer with CNT arrays placed into the square holders, the carrier consists of two silicon wafers patterned and etched to fit atop each other with windows exposing the CNT arrays placed between them, the carrier shown in Figure 3 is the bottom and will be covered by a top wafer to secure the wafers in place preventing any slippage into the cleanroom tools.

### Conclusions and Future Steps:

Optimizing ion mill parameters and developing a carrier wafer to hold pieces led to an increase in production yield. Further studies are to be conducted to optimize other clean room processes that are utilized in the fabrication of these devices.

### References:

- [1] Siddiqui, Mujtaba Yar Khan, "Application of ICP RIE Techniques to Produce CNT Arrays" (2023). Thesis. Rochester Institute of Technology. Accessed from: <https://repository.rit.edu/theses/11656>.
- [2] Golshadi, Masoud, "Carbon Nanotube Arrays for Intracellular Delivery and Biological Applications" (2016). Thesis. Rochester Institute of Technology. Accessed from: <https://repository.rit.edu/cgi/viewcontent.cgi?article=10360&context=theses>.

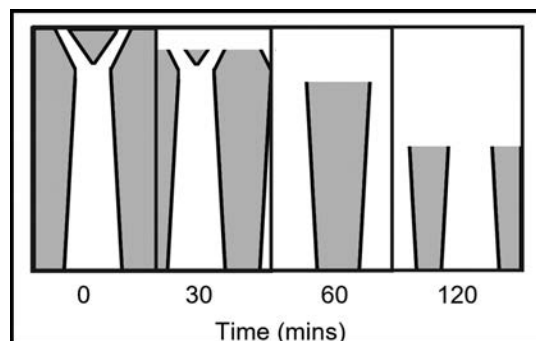


Figure 2: Schematic depicting effect of ion mill time on lattice layer evolution.

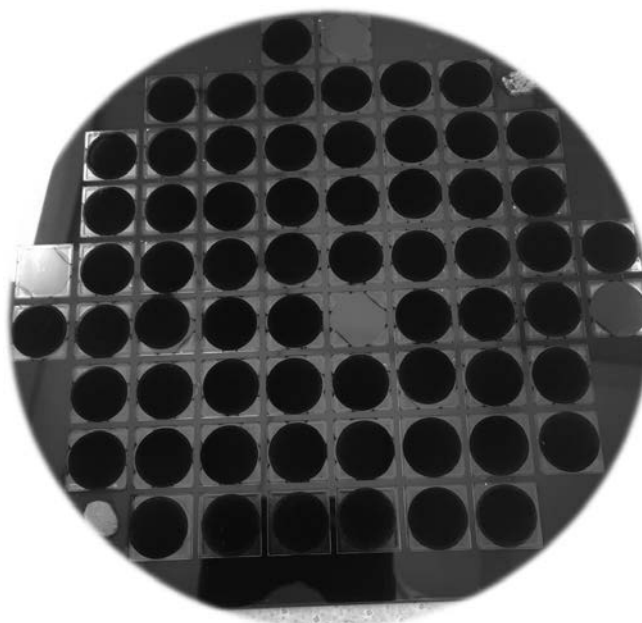


Figure 3: Silicon carrier wafer to hold CNT arrays during cleanroom fabrication.

# High-Density, Integrated, Multi-Functional Neural Probe for Small Animals

**CNF Project Number: 3135-23**

**Principal Investigator(s): Azahara Oliva Gonzalez, Antonio Fernandez-Ruiz**

**User(s): Lindsay Karaba, Jaehyo Park, Zifang Zhao**

*Affiliation(s): Neurobiology and Behavior, Cornell University*

*Primary Source(s) of Research Funding: DP2MH136496(NIH), R00MH120343(NIH), R00MH122582(NIH)*

*Contact: aog35@cornell.edu, afr77@cornell.edu, lak256@cornell.edu, jp2597@cornell.edu, zz833@cornell.edu*

*Research Group Website: braincomputation.org*

*Primary CNF Tools Used: Parylene Coater, SUSS MA6|BA6 Aligner, Nanoscribe GT2 Two-Photon Lithography System, Heidelberg DWL2000, CHA Mark 50 E-beam Evaporator*

## Abstract:

Micro-fabricated neural probes serve as an important tool for probing neural activities. There is an increasing need for developing high-density, multi-functional devices for monitoring electrical and electrochemical signals with minimal invasive and long-operation time in physiological environments. We have designed and fabricated a high-density neural interface in a conformable parylene-C substrate. Our probe has a cross-section of  $3 \times 126 \mu\text{m}^2$ , ensuring low damage to brain tissues. To achieve wireless neural activity recording in rodents during unrestrained behavior, we designed a light-weight wireless high-channel count headstage and performed parylene coating to ensure all-weather operations. We used a low-temperature solder bonding process to achieve high-density soft-hard circuit bonding, which enables connector-free, direct integration of the probe to a circuit board that allows a total system weight  $< 4$  grams. With this system, we successfully recorded high-quality data from a freely moving animal in a naturalistic environment.

## Summary of Research:

Recent advances in neural interfaces enabled recording of high-resolution neural activities up to a few thousand channels [1]. However, most high-density neural interfaces are built with rigid, silicon-based substrates [2].

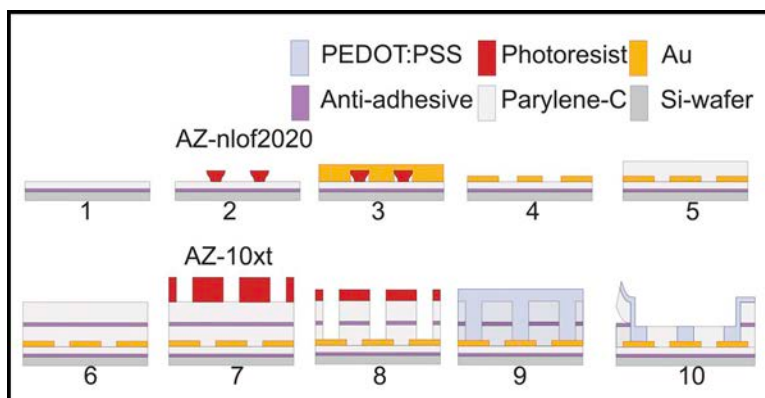


Figure 1: Microelectrode fabrication processes.

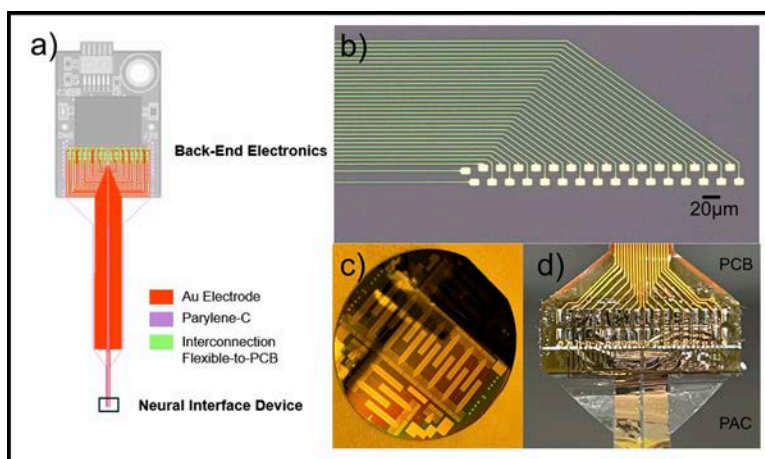


Figure 2: Light-weight, high-density neural probe. a) Illustration of wireless, light-weight neural monitor system. b) High-density, microelectrode on parylene substrate. c) 27 electrodes fabricated in a 4-inch wafer. d) soft-rigid electronic bonding with low-temperature solder.

This leads to physical damage to brain tissue during implantation and micro-electrode movement, and eventually degraded the signal quality. In order to solve this, we are building implantable microelectrodes with conformable, organic materials. We fabricated high-density conformable neural probe with parylene-C with similar process as previously reported [3] (Figure 1). In short, we used metal lift-off process to pattern a 150 nm Au layer on parylene-C substrate, then used dry etching process to pattern the opening in parylene-C passivation layer. We designed high-density neural probe with stackable design with 32ch in each probe unit to be directly bonded with back-end electronics (Figure 2a). Using CNF, we have optimized the lift-off process to reduced interconnect line width to 3  $\mu\text{m}$  (Figure 2b). To achieve effective electrical bonding between parylene-C based neuro probe to a printed circuit board, we used a low-temperature solder bonding processing with a low melting point solder paste (137°C). We achieved reliable bonding without damaging parylene substrate (Figure 2c). Direct bonding of microelectrode and back-end circuit removed the need for complicated bonding process or bulky connectors and lead to a reduced form factor and system weight. We achieved 1.86 grams total system weight, with additional 2 grams for the lithium battery. This system could wirelessly record neural activity with a configurable channel number ranging from 64 channels to 256 channels. We used parylene-C for coating the back-end device for weather-proof coating. This allows us to record in freely moving rodents in outdoor, naturalistic environment in Liddel field campus. With this system, we have recorded high-quality electrophysiology signal in both rat and mouse hippocampus, to study the learning and memory function of related neural networks.

## Conclusion and Future Steps:

We have fabricated conformable, high-density micro-electrodes with CNF tools and they have advanced our capability of study animal neural activity in traditionally challenging, unconventional environments. In the future, there are many possible directions we could work on to extend this work.

1) Multi-modal sensing: Currently, we are only using passive electrode to record electrical activity produced by neurons. Neural networks also rely on chemical signaling system, such as neurotransmitters. We are looking into how to effectively use different materials to electrically interact with neurotransmitters to actively sense the concentration of neurotransmitters, with multi-channel electrodes.

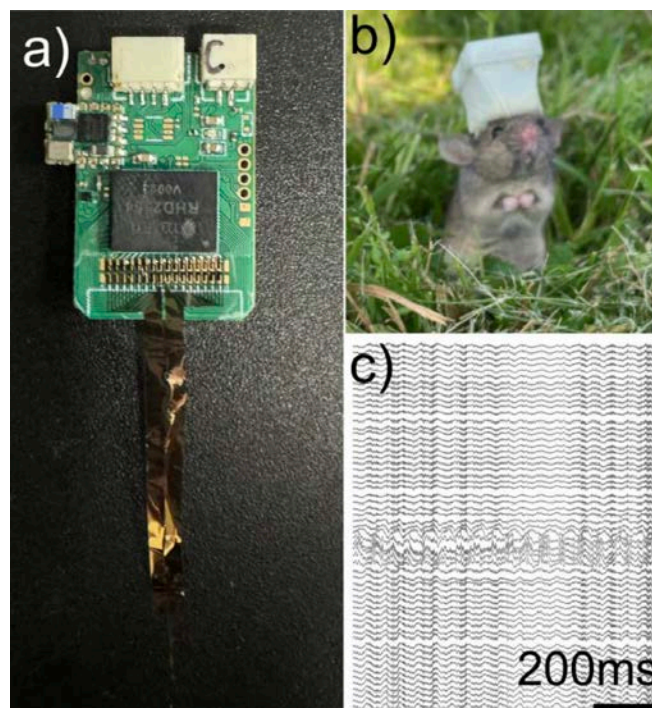


*Figure 3: Wireless electrophysiology system for study unbounded animal behavior. a) Assembled wireless device with microelectrodes. b) A mouse with 3D printed carrier for wireless headstage. c) Recorded high quality electrophysiology during animal locomotion.*

2) Neuro-modulations: Neuroscience also require tools to perturb neural circuits to investigate its functions. Importantly, optogenetics can modulate a subgroup neuron's function through opto-stimulation. We are currently exploring the possibility to build thin-membrane microelectrode on top of a thin wave-guide with the NanoScribe.

## References:

- [1] Jun, J. J., et al. Fully integrated silicon probes for high-density recording of neural activity. *Nat.* 2017 5517679 551, 232-236 (2017).
- [2] Chen, R., Canales, A., and Anikeeva, P. Neural recording and modulation technologies. *Nat. Rev. Mater.* 2017 22 2, 1-16 (2017).
- [3] Zhao, Z., Cea, C., Gelinis, J. N., and Khodagholy, D. Responsive manipulation of neural circuit pathology by fully implantable, front-end multiplexed embedded neuroelectronics. *Proc. Natl. Acad. Sci. U. S. A.* 118, e2022659118 (2021).